Lan *et al. Cell Communication and Signaling* (2025) 23:137
https://doi.org/10.1186/s12964-025-02146-7

Cell Communication
and Signaling

**RESEARCH** **Open Access**

# Combination therapy with Chicoric acid and PD-1/PD-L1 blockade improves the immunotherapy response in patient-derived ovarian cancer xenograft model

Hongwei Lan[1], Jingjuan Zhu[1], Helei Hou[2], Chuantao Zhang[2], Xingfa Huo[1], Yuming Zhang[1], Fangfang Yang[1], Na Zhou[1*] and Xiaochun Zhang[1*]

**Abstract**

**Purpose** Limited treatment options exist for refractory ovarian cancer (OC) due to its poor response to immune therapies. Therefore, there is an urgent need to develop new effective treatment strategies. Chicoric acid (CA) is reported to have immune-enhancing properties, but its efficacy in cancer treatment is not well understood. We hypothesize that CA might improve the efficacy of PD-1/PD-L1 blockade immunotherapy in refractory OC patients.

**Methods** Patient-derived xenograft (PDX) models were constructed from chemoresistant advanced high-grade serous ovarian cancer patients. These models were treated with CA, aPD-1/aPD-L1 antibodies, or a combination of both. Single-cell RNA sequencing was performed to analyze the cellular composition of the tumor microenvironment (TME), evaluate treatment efficacy, and explore therapeutic mechanisms. Variations in peripheral blood lymphocytes were analyzed via fluorescence-activated cell sorting. Immunohistochemistry confirmed the variations in tumor-infiltrating lymphocytes and tumor cells.

**Results** Immunocompetent peripheral blood mononuclear cell (PBMC)-PDX models were successfully constructed using malignant ascites fluid and PBMCs. After treatment, 158,734 cells from 15 samples were categorized into epithelial cells, T lymphocytes, myeloid cells, fibroblasts, and endothelial cells. CA enhanced the antitumor ability of immune cells against OC cells. Notably, CA stimulated the proliferation of CD45 + and CD3 + cells and promoted the migration of CD8 + and CD4 + T cells from peripheral blood to infiltrate the TME. Additionally, CA enhanced the response of OCs to aPD-L1/aPD-1 treatment, strengthened the interaction between tumor and nontumor cells, and identified APP/CD74 as a critical ligand–receptor pair. CHI3L1 was also found to be a potential marker for predicting immunotherapy efficacy in OC.

**Conclusion** This study demonstrated that combination therapy with CA and aPD-1/aPD-L1 might be a promising strategy for treating OC effectively.

*Correspondence:
Na Zhou
zhouna@qdu.edu.cn
Xiaochun Zhang
zxc9670@qdu.edu.cn

Full list of author information is available at the end of the article

**Keywords** Ovarian cancer, Immunotherapy, Chicoric acid, PBMC-PDX, Single-cell RNA sequencing

## Introduction

High-grade serous ovarian cancer (HGSC) is the most common and lethal histological subtype of ovarian cancer (OC), accounting for approximately 80% of OC-related deaths [1, 2]. Despite initial responses to cytoreductive surgery and systemic chemotherapy, HGSC is incurable, as recurrence and chemotherapy resistance occur in most cases, resulting in an overall 5-year survival rate of less than 40% [3–5]. Owing to advancements in precision medicine, immune checkpoint blockade (ICB) drugs have shown impressive efficacy in treating solid tumors such as lung cancer, bladder cancer, and melanoma; however, as a type of "cold tumor," HGSC unfortunately responds poorly to these drugs [6–8]. Specifically, why this is the case remains poorly understood, highlighting the need to study the underlying biology of immune evasion in ovarian cancer using optimal animal models. Unfortunately, the preclinical models required to address questions regarding the contributions of specific HGSC-specific characteristics to immune evasion have been limited until now [9].

The substantial heterogeneity present within the tumor microenvironment (TME) continues to pose a challenge in the comprehension and treatment of cancer, and reports suggest that TME-targeted therapy may turn "cold tumors" into "hot tumors" to achieve a better response rate to ICB treatment [10]. Therefore, gaining a comprehensive understanding of the dynamic functional interactions within this complex environment holds great potential for guiding the development of effective combinatorial approaches against cancer. The patient-derived xenograft (PDX) model, which has been proven to be effective at simulating the characteristics of cancer cells in the tumor microenvironment (TME) and maintaining close similarities to the original tumor in terms of cell phenotype, molecular features, cell−cell interactions in the TME, and clinical outcome prediction, is prevalent in precision medicine [11, 12]. PDX models have been used to evaluate drug efficacy in multiple types of cancer [13–16], and they have been applied in several HGSC studies, which have demonstrated their value for researching this deadly disease [17–21]. However, the application of immunocompetent PDX models is rare [9]. Single-cell RNA sequencing (scRNA-seq) transcriptional profiling is becoming a powerful tool for dissecting the complexity of the HGSC TME because it can accurately distinguish cell heterogeneity and gene regulatory networks and identify distinct functional cell subpopulations [22–26].

Chicoric acid (CA) is a derivative of caffeic acid and is extracted from the plants *E. purpurea*, *E. angustifolia*, and *E. pallida* [27]. CA has been used to treat diseases such as the common cold, bronchitis and upper respiratory infections because of its antioxidative, anti-inflammatory, antibacterial properties [28, 29]. However, the effectiveness of CA in cancer treatment has largely relied on anecdotal evidence [30, 31], with limited direct data on its efficacy and the specific mechanisms underlying its potential antitumor effects. For example, in gastric cancer research, Sun X et al. [32] found that CA significantly reduced gastric cancer cell activity in vitro and slowed tumor growth while reducing tumor volume in animal models. In colon cancer, CA induced notable cytotoxicity and strongly inhibited cancer cell growth, ultimately leading to tumor cell apoptosis [33]. Furthermore, CA has been shown to enhance immune responses. In a study with chronically stressed mice, CA significantly enhanced lymphocyte proliferation and increased populations of CD3+, CD4+, and CD8 + T cells. It also upregulated CD28 and CD80 while downregulating CTLA-4, thereby stimulating the immune system [34]. Another report demonstrated that CA can further enhance the immune response by modulating natural killer (NK) cell activity [35]. Based on these findings, we hypothesize that CA might enhance the efficacy of tumor immunotherapy. To test this hypothesis, we designed the current study.

In this study, we evaluated the efficacy of aPD-1/aPD-L1 antibodies and CA via the construction of an immunocompetent PDX model and subsequent comprehensive analysis of the TME (Fig. 1A). Although HGSC is insensitive to immune checkpoint inhibition alone, the combination of CA and aPD-1/aPD-L1 antibodies has demonstrated antitumor effects in a preclinical model. Our results provide valuable insights for the development of immunotherapy strategies and could guide future immunotherapy approaches for HGSC.

## Results

### Construction of the PBMC-PDX model by injecting human Ascites fluid and PBMCs

The first-generation PDX model (P0) was established by injecting immunodeficient NSG mice with malignant ascites obtained from a chemotherapy-resistant, refractory advanced HGSC patient who experienced relapse and progression after undergoing tumor debulking surgery and multiple systemic chemotherapies (Fig. S1A, S1B; Methods). Histopathological similarity between P0 and the parent tumor was confirmed through pathological diagnosis by a pathologist, and the ability of the PDX to maintain histological similarity during the passage process was also validated in P1, P2, and P3 (Fig. 1B).

The reliability of obtaining tumor-infiltrating lymphocytes (TILs) by culturing reactive T cells with peripheral blood mononuclear cells (PBMCs) and from established PDXs has been previously demonstrated [36]. To optimize the use of PDXs for assessing the efficacy of ICB, we constructed an immunocompetent PDX model by injecting processed patient-derived PBMCs ($5 \times 10^6$/mouse via intraperitoneal injection). Compared with that in the control group, the proportion of CD45 + CD3 + cells in the PBMC-PDX group was significantly greater (Fig. 1C and D and S1C), and the body weight of the PBMC-PDX model group was not obviously different from that of the control group (S1D), which suggested the tolerance of the mice to the PBMC-PDXs. Notably, the tumor volume and tumor weight of the PBMC-PDX model group were not significantly reduced, indicating successful construction of an immune-suppressive tumor immune microenvironment (TIME), which is similar to patient conditions (Fig. 1E and F, S1E). We subsequently demonstrated that the PD-L1 expression level and genetic alterations in the PBMC-PDX tumors were similar to those in the original tumors.

Finally, we randomly assigned 30 PBMC-PDX model mice to 6 groups (5 mice per group) and treated them with different regimens to evaluate the synergistic effects of CA and ICB immunotherapy (Supplementary 1), their impact on the TME, and the underlying mechanisms, with the ultimate goal of identifying effective treatment strategies for HGSC.

### CA enhances the HGSC response to PD-L1/PD-1 antibodies

We evaluated the therapeutic effects of the aPD-L1 drug atezolizumab and the aPD-1 drug toripalimab. Compared with the control treatment, atezolizumab treatment resulted in a slight decrease in tumor volume (TGI = 28.04%, $P = 0.51$), whereas toripalimab led to a rapid and sustained reduction in tumor size, resulting in a significant decrease (TGI = 79.88%, $P = 0.0006$) (Fig. 2A). To explore superior immunotherapeutic strategies, we assessed the impact of CA, which is known for its immunoenhancing properties.

Through cell experiments, we found that while CA could not directly inhibit OC cell proliferation, it could stimulate PBMC proliferation and enhance the cytotoxic effect of immune cells on tumor cells (Fig. 2B, C and D). We plan to further validate these findings via a PBMC-PDX model. Initially, we determined that 50 mg/kg is the optimal treatment dose for CA (Fig. 2E), which consistent with previous studies [32]. Interestingly, we observed an increase in tumor volume following CA treatment compared with that in the control group (TGI = -26.99%, $P = 0.18$) (Fig. 2F, S2A). However, we noted an increase in CD45 + cells after CA treatment on days 10 and 14 (Fig. 2G, S2B). On this basis, we hypothesize that CA may increase the therapeutic efficacy of aPD-L1/PD-1 treatment.

To test this hypothesis, we administered CA in combination with aPD-L1/PD-1 to PBMC-PDX models. The results revealed a substantial decrease in tumor volume in both the atezolizumab + CA group (TGI = 74.70%, $P = 0.035$) and the toripalimab + CA group (TGI = 72.20%, $P = 0.013$) compared with the control group (Fig. 2F, S2A). However, compared with aPD-1 monotherapy, the aPD-1 + CA combination did not further reduce tumor volume or tumor weight (Fig. 2F, S2A, S2C, S2D). To investigate this further, we performed single-cell sequencing analysis.

### Cellular composition of the HGSC TME revealed by scRNA-seq analysis

Fifteen samples were utilized for scRNA-seq analysis following standard procedures via the BD Rhapsody platform (Methods). After quality filtering, a total of 158,734 cells were obtained (Fig. S3A, S3B). Dimensionality reduction and cell clustering classified the cells into 20 clusters, of which expressed expressing different marker genes (Fig. 3A, S3C). Five cell types were identified based on the basis of cluster-cluster Pearson correlation and signature gene expression (Fig. 3B C, 3D), including epithelial cells (marked by EPCAM, KRT18), T lymphocytes (marked by CD3D, CD3E), myeloid cells (marked by CD68, C1QB), fibroblasts (marked by COL1A1, COL1A2), and endothelial cells (marked by VWF, AQP1) (Fig. S3D). Among all the samples, epithelial and myeloid cells were the predominant cell types, followed by T lymphocytes, with the stromal compartment consisting of fibroblasts and endothelial cells (Fig. 3E). Additionally, we observed that different treatments led to distinct variations in cell proportions (Fig. 3F), warranting further analysis.

### Heterogeneity and variation in epithelial cells after treatment

We used inferCNV analysis to investigate the genetic status of epithelial cells and found that all the cells were malignant (Fig. 4A). To explore this heterogeneity systematically, we classified epithelial cells into nine subtypes on the basis of enrichment analysis and gene expression profiling (Fig. 4B).

EC1 and EC2 are associated with cell growth pathways, with EC1 involved in mitosis and EC2 involved in DNA replication (Fig. S4A). EC3, potentially located on the tumor surface, plays an important role in intercellular connectivity, as it is enriched in the apical junction and apical surface pathways. Furthermore, EC1, EC2, and EC3 are relatively normoxic cells likely located in areas with ample blood supply and energy. Conversely, EC8, enriched in the hypoxia pathway, exhibited strong glucose metabolism and a weakened TCA cycle (Fig. S4A), indicating that it primarily obtains energy through

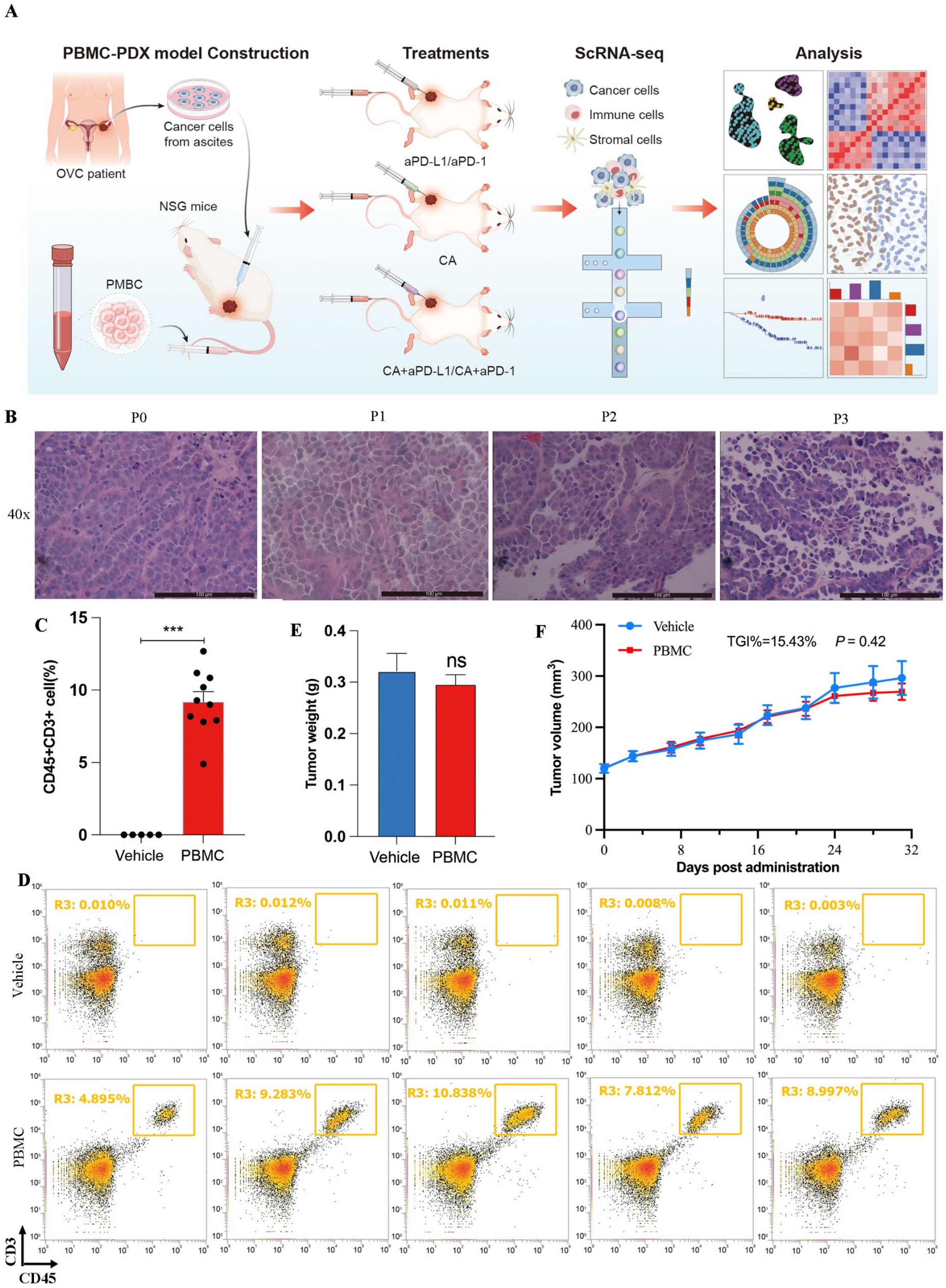

**Fig. 1** Construction of PBMC-PDXs. (**A**) Schematic overview of the study design and analytical workflow. (**B**) Pathological hematoxylin and eosin staining of the 0th, 1st, 2nd, and 3rd generations of the PDX model. (**C**, **D**) Levels of CD45 + CD3 + cells in the peripheral blood of PDX model mice after PBMC injection. *** indicates $P < 0.001$, ns indicates $P > 0.05$ (applied to all subsequent figures). (**E**) Comparison of tumor weight between the control and the PBMC injection groups. (**F**) Comparison of tumor volume between the control and PBMC injection groups

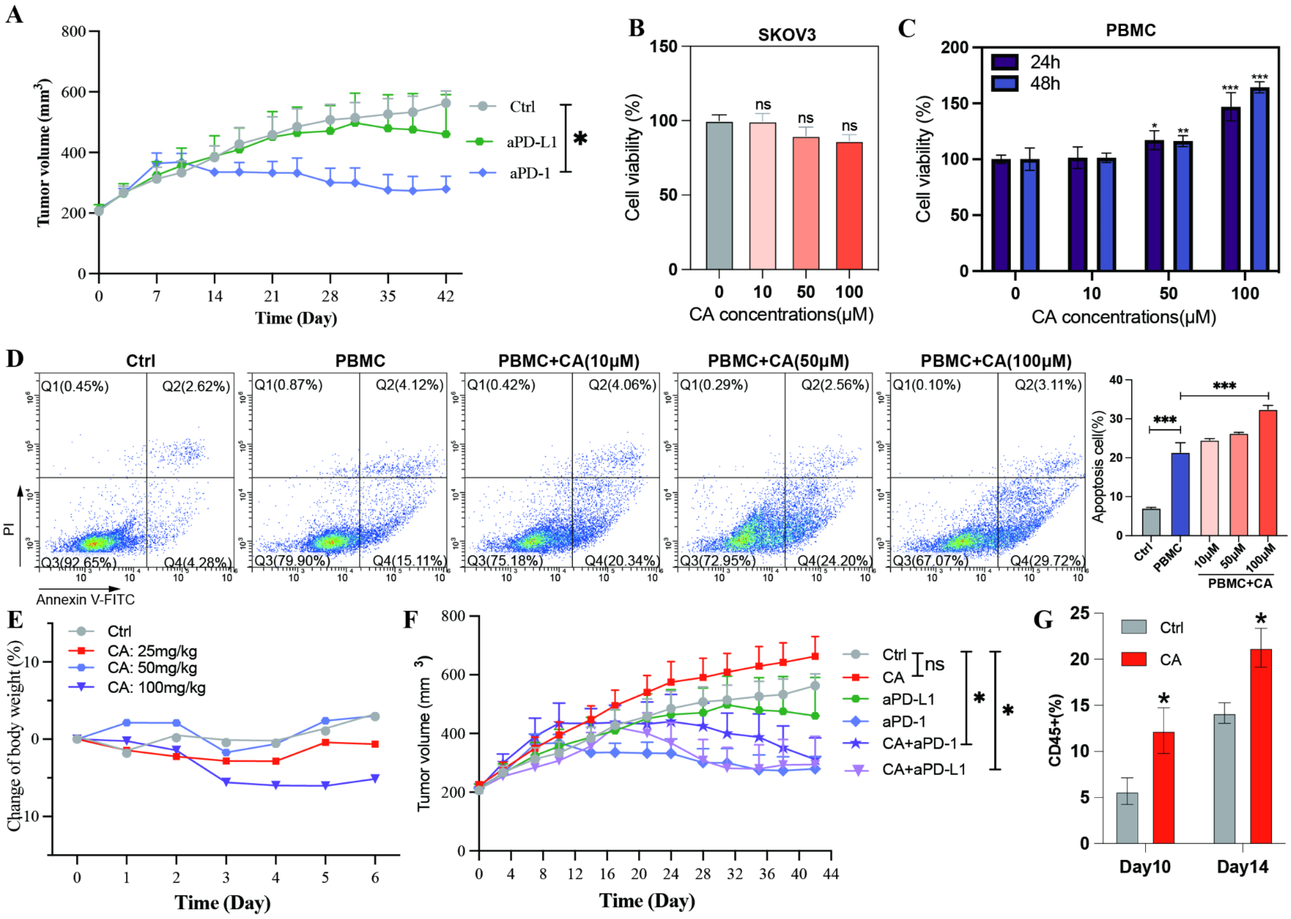

**Fig. 2** Evaluation of different treatment regimens in vitro and in vivo. (**A**) Comparison of tumor volume among the control, anti-PD-L1 (aPD-L1) treatment, and anti-PD-1 (aPD-1) treatment groups. (**B**, **C**) CCK-8 assay showing the impact of CA (0, 10, 50, 100 μM) on the viability of SKOV3 cells and PBMCs. * indicates $P < 0.05$, ** indicates $P < 0.01$, and *** indicates $P < 0.001$ compared with the control group (applied to all subsequent figures). (**D**) Flow cytometry analysis showing the impact of CA + PBMC on the apoptosis of SKOV3 cells. (**E**) Weight change in mice treated with different doses of CA. (**F**) Changes in tumor volume among the different groups. (**G**) Comparison of CD45 + cells after treatment with CA on days 10 and 14

anaerobic glycolysis. These findings suggest that EC8 cells are hypoxic and possibly located in the central core of the tumor or poorly vascularized regions and possess greater invasive and migratory potential than do EC1, EC2, and EC3 cells [37, 38]. EC5 and EC6 are associated with tumor cell immunoreaction and inflammation (Fig. S4A). Additionally, although EC4 was not involved in specific signaling pathways, these cells highly expressed the tumor invasion- and metastasis-related gene THSD4 (Fig. S4B) [39], and EC7 was also enriched in tumor invasion and migration processes or pathways (Fig. S4C).

EC2 and EC7 had lower CNV scores, whereas EC3, EC6, EC8, and EC9 had higher scores (Fig. 4C). Pseudotime analysis revealed that EC1 and EC2 appeared in multiple developmental branches but were present primarily at early developmental stages with low differentiation (Fig. 4D and E F, S4D, S4E). EC8, at the developmental endpoint, had the greatest degree of differentiation, driven by malignancy-associated genes such as MYC, CXCR4, CD44, and VEGFA, indicating that EC8 is a mature, highly malignant tumor cell type (Fig. 4E F, S4F, S4G). These findings suggest that EC1, EC2, and EC3 are more therapy sensitive, whereas EC8 shows greater treatment resistance and invasive potential [40, 41].

The proportion of tumor cells did not significantly decrease after aPD-1 treatment but increased with aPD-L1 treatment. Compared with the control treatment, CA treatment reduced the tumor cell proportion. Compared with the control treatment, CA + aPD-L1 treatment resulted in a greater proportion of tumor cells but a lower proportion than did aPD-L1 treatment alone. CA + aPD-1 treatment had the lowest proportion, indicating the best efficacy (Fig. 4G). These treatments also altered tumor cell subtypes. aPD-L1 and CA + aPD-L1 therapies decreased the number of EC1 and EC2 cells but increased the number of EC8 cells, whereas aPD-1 and CA + aPD-1 had the opposite effect (Fig. 4H). Compared with the control, CA treatment resulted in a greater proportion of EC3 cells, with similar trends in the CA + aPD-L1 and CA + aPD-1 groups compared with the

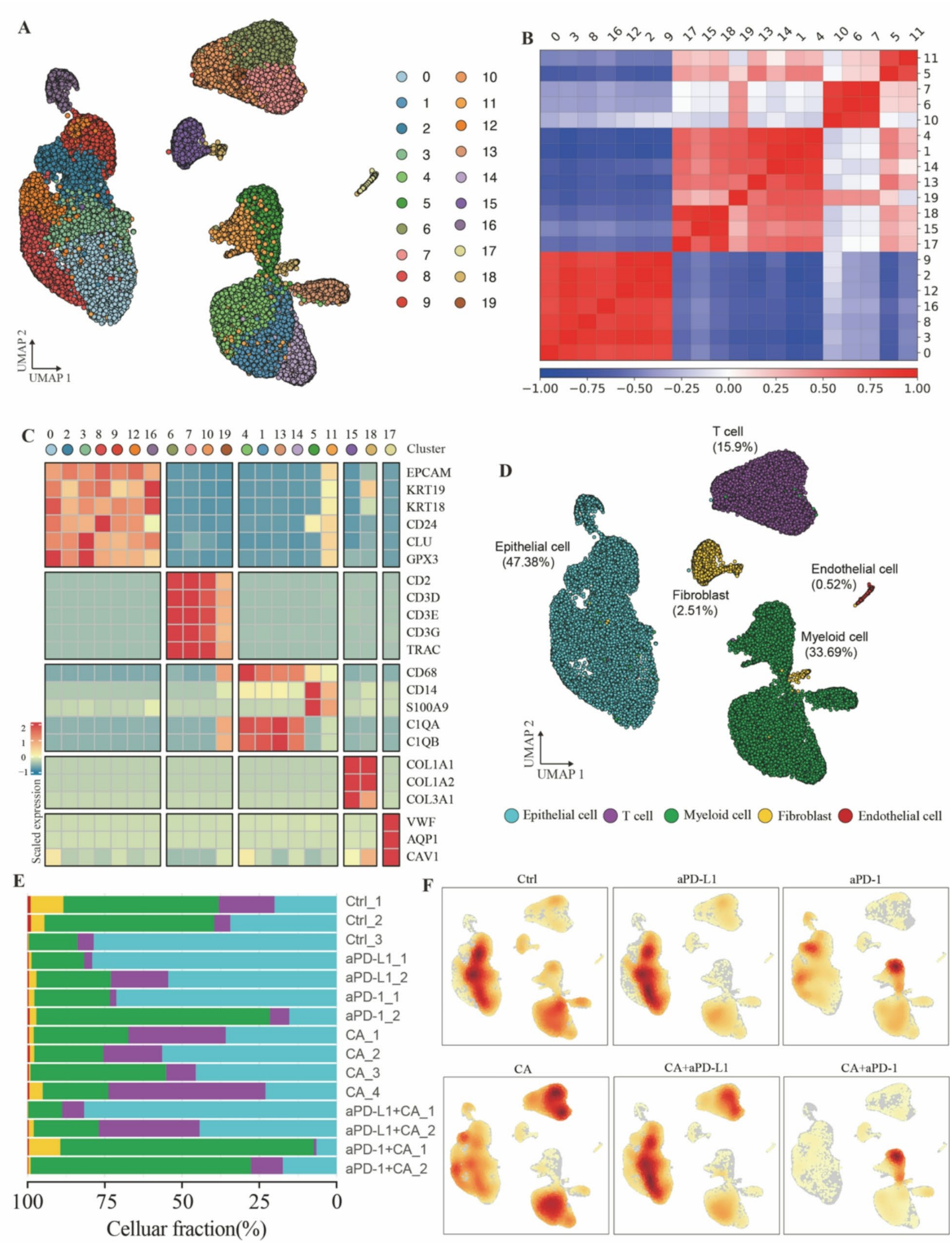

**Fig. 3** Identification of cell types in the HGSC microenvironment. (**A**) Uniform Manifold Approximation and Projection (UMAP) showing all the cell clusters. (**B**) Heatmap showing the Pearson correlation among clusters. (**C**) Heatmap showing the unique expression of marker genes in clusters. (**D**) UMAP showing five main cell types. (**E**) Proportion of five cell types across all samples. (**F**) Density plot showing the distribution of cell numbers across different groups

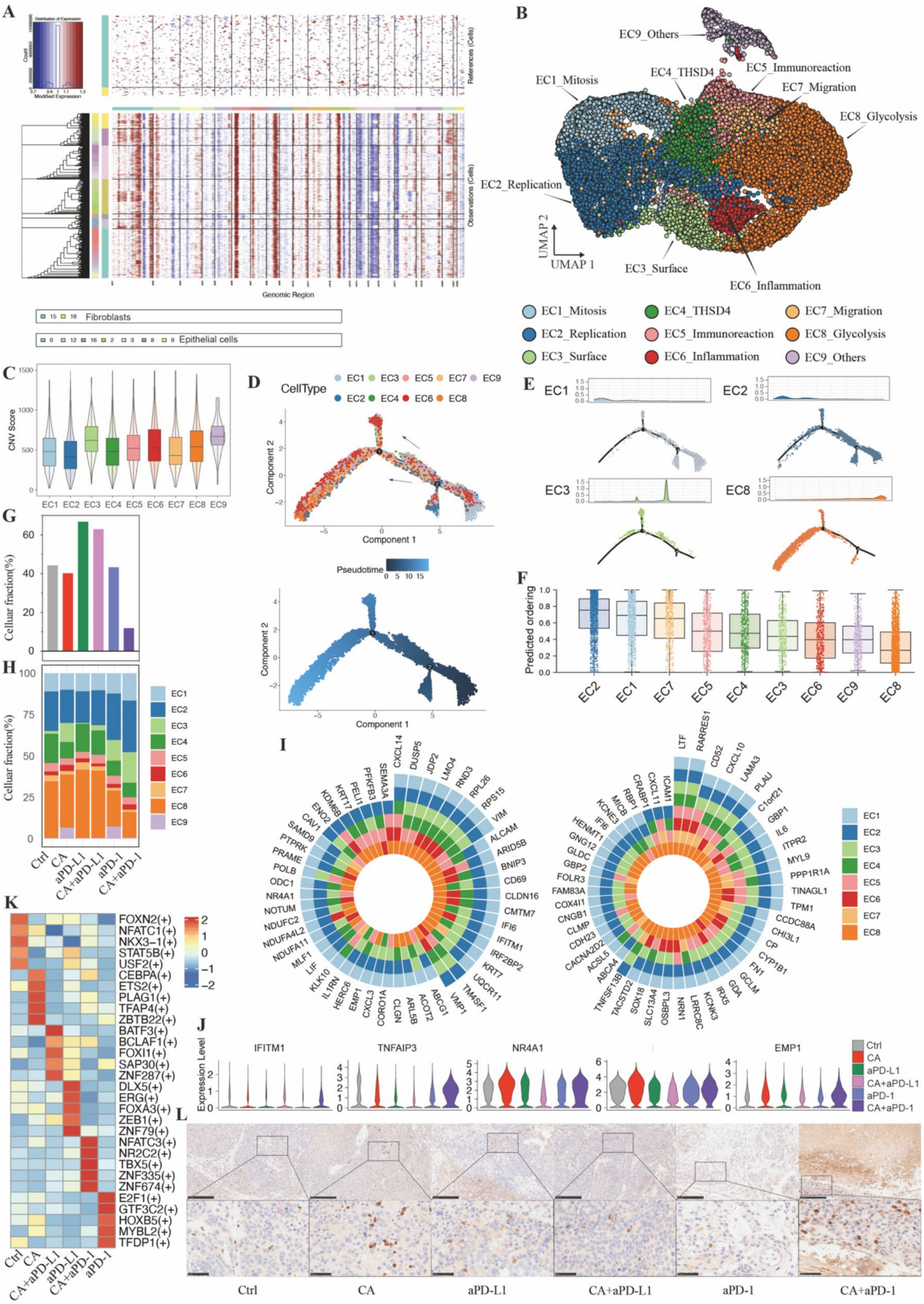

**Fig. 4** (See legend on next page.)

(See figure on previous page.)

**Fig. 4** Heterogeneity and variation of epithelial cells in the HGSC microenvironment. (**A**) Hierarchical heatmap of InferCNV analysis showing large-scale CNVs in epithelial cells. (**B**) UMAP visualization of epithelial cell subtypes. (**C**) CNV scores of epithelial cell subtypes. (**D**, **E**) Pseudotime trajectory analysis of epithelial subtypes. (**F**) Differential levels of epithelial subtypes. (**G**, **H**) Proportion of epithelial cells and epithelial cell subtypes in different groups. (**I**) Differentially expressed genes (DEGs) between CA + aPD-L1 and aPD-L1 (left) and between CA + aPD-1 and aPD-1 (right). (**J**) Violin plots showing the expression levels of DEGs among the different groups. (**K**) Top 5 most activated transcription factor regulons of epithelial cells among the different groups. (**L**) IHC showing the expression level of PD-L1 in the different groups

monotherapy group, indicating the antitumor efficacy of CA (Fig. 4H).

A generalized linear model revealed that CA enhanced aPD-L1 and aPD-1 effects by inducing the expression of tumor-suppressive genes such as IFITM1, TNFAIP3, NR4A1, and EMP1 (Fig. 4I and J). Posttreatment changes in cell types and gene expression led to biological differences in tumor cells. CA treatment enhanced immune-related pathways while reducing the proliferation pathway, which was consistent with the results of the cell experiments (Fig. S4H). In contrast, aPD-L1 treatment increased hypoxia pathway enrichment, which was mitigated by CA. aPD-1 treatment increased cell proliferation and reduced hypoxia, and these effects were amplified by CA along with increased inflammation pathway enrichment (Fig. S4H). Additionally, we found that the CA + aPD-1 group presented increased activity of regulons associated with the immune response, such as those regulated by NFATC3, ZNF335, NR2C2, and AHR (Fig. 4K).

Finally, low PD-L1 and PD-L2 positivity in the TME might explain the poor efficacy of aPD-L1 treatment, whereas the better efficacy of aPD-1 could be attributed to other factors (Fig. 4L, S4I).

## CA enhances T lymphocyte proliferation and infiltration into the TME

T lymphocytes are the main immune cells involved in immune checkpoint blockade (ICB) treatment. In this study, T cells were classified as CD4 or CD8 T cells on the basis of CD4 and CD8A gene expression, with further subdivisions into subtypes (Fig. 5A and B). CD8 + T cells were categorized as cytotoxic (CD8-GZMH and CD8-FGFBP2), dysfunctional (CD8-CXCL13), or proliferating (CD8-TOP2A and CD8-PCNA) cells. CD4 + T cells were classified as naïve memory (CD4-IL7R), dysfunctional (CD4-CXCL13), regulatory (CD4-FOXP3), or proliferating (CD4-TOP2A) (Fig. 5A and C). Proliferating CD4 + and CD8 + T cells can develop into exhausted and cytotoxic cells, respectively, via different branches (Fig. S5A, S5B). The proportions of tumor-infiltrating lymphocytes (TILs) significantly increased after CA treatment. Compared with aPD-L1/aPD-1 alone, the combination treatment also increased the TIL proportion, although the TIL proportion in the aPD-1/CA + PD-L1 treatment group was lower than that in the PD-L1/CA + PD-L1 treatment group (Fig. 5D). Immunohistochemistry (IHC) confirmed the increase in CD8 + TILs (Fig. 5F). Additionally, a decrease in the CD8/CD4 cell ratio was observed in the combination treatment groups compared with the monotherapy groups, accompanied by a reduction in CD8_CXCL13 and CD8_GZMH, likely because CA enhances the tumor-killing ability of CD8 + T cells, leading to partial consumption of these cells (Fig. 5E).

We investigated the source of the increased number of TILs and found an increase in the number of CD45 + cells after CA treatment by day 14 compared with that in the controls; however, both the number of CD45 + and the number of CD3 + cells decreased by day 42. Similar trends were observed in the CA + aPD-L1 and CA + aPD-1 groups, whereas the number of immune cells in the aPD-L1 and aPD-1 monotherapy groups was lower than that in the control group at both day 14 and day 42 (Fig. 5G and H, S5C). Thus, we believe that aPD-L1/aPD-1 treatment facilitates lymphocyte migration to the TME, a process that is enhanced by CA. The tumor enlargement observed in the CA group is likely due to pseudoprogression resulting from increased TILs.

Additionally, immune-related pathways in the TME, such as the IL6-JAK-STAT3/IL2_STAT5 signaling pathway and the interferon-gamma response, and complement activation. Compared with monotherapy, CA + aPD-1/CA + aPD-L1 therapy resulted in similar trends. Despite the lower T lymphocyte proportion in the aPD-1/CA + aPD-1 group, the enrichment of immune-related pathways was greater than that in the aPD-L1/CA + aPD-L1 group (Fig. 5I). To explore the variation in the state of CD8 T cells, we selected the top 50 genes most correlated with LAG3 to determine the dysfunction score and the top 50 genes associated with GNLY to compute the cytotoxicity score. (Fig. 5J and K, S5D). After CA treatment, the dysfunction score of CD8 + T lymphocytes decreased, whereas the cytotoxic score increased. Following CA + aPD-L1 and CA + aPD-1 treatments, dysfunction scores decreased, particularly for CA + PD-1, but activation scores did not increase (Fig. 5L). In summary, CA increases the TIL proportion and enhances the immune-killing environment in the TME, not by increasing the number of cytotoxic cells or reversing the number of exhausted cells but rather by recruiting fresh TILs.

### CHI3L1 + cells serve as predictive markers for immunotherapy efficacy in OC

In addition to tumor cells, myeloid cells are the most abundant cell type in the TME. We further classified myeloid cells into 13 groups, including neutrophils, tumor-associated macrophages (TAMs), and mast cells (Fig. 6A). TAMs, one of the most prevalent immune cell types in the TME, were divided into 11 subtypes on the basis of characteristic gene expression (Fig. 6A and B). These cell types express different marker genes and are involved in distinct biological processes (Fig. 6B). Pseudotime analysis revealed that Macro-TOP2A and Macro-SPP1 displayed relatively low differentiation levels and could differentiate into other TAM subtypes under certain conditions, whereas neutrophils presented the greatest degree of differentiation, which was consistent with their highly differentiated characteristics (Fig. 6C and D, S6A).

Posttreatment, the proportion of myeloid cells varied: it decreased in the CA, aPD-L1, and CA + aPD-L1 groups, with a reduction in the number of neutrophils and increases in the number of Macro-FN1, Macro-APOE, and Macro-SPP1 cells (Fig. 6E and F). Conversely, the myeloid cell proportion significantly increased in the aPD-1 and CA + aPD-1 groups, with the most notable increase in neutrophils (Fig. 6E and F).

CHI3L1 + cells, including neutrophils, CHI3L1_TAMs, and VCAN_TAMs, were the most different cell types between the aPD-1/CA + aPD-1 and PD-L1/CA + aPD-L1 groups (Fig. S6B, 6G). CHI3L1 + cells highly expressed IL1B and IRF1, indicating their primary antitumor role in the TME (Fig. 6G). These shifts in cell composition led to distinct myeloid cell pathway enrichment among the different treatment groups (Fig. S6C). CHI3L1 is expressed in tumor cells, fibroblasts, and myeloid cells, with the highest expression level observed in myeloid cells (Fig. S6D, S6E). Notably, its expression peaked in the CA + aPD-1 group and was lowest in the aPD-L1 group (Fig. 6H). Additionally, CHI3L1 was negatively correlated with T lymphocyte and CD8 T lymphocyte proportions in the TME, and there was mutual exclusivity between CHI3L1 and CD8 lymphocytes, which may partly explain the lower number of TILs in the aPD-1/CA + aPD-1 group (Fig. 6I, J and K).

Further data revealed that CHI3L1 expression in OC is significantly higher than that in normal tissues and is negatively correlated with OC prognosis (Fig. S6F, S6G, S6H) [42, 43]. However, an analysis of data from the Kaplan−Meier plotter database [44] revealed that higher CHI3L1 levels were associated with better immunotherapy outcomes and were significantly correlated with aPD-1 and aPD-L1 treatments but not with aCTLA-4 treatment in cancer patients receiving immunotherapy (Fig. 6L and M, S6I). These findings suggest that the expression of CHI3L1, similar to that of PD-L1, may help in evaluating immunotherapy efficacy. Additionally, we found that CHI3L1 can be secreted into the TME (Fig. S6J), which aligns with reports of its high blood levels, further supporting its potential as an easily accessible immunotherapy biomarker.

Overall, these findings indicate that the proportion of CHI3L1 + cells increased, whereas the proportion of TAMs decreased after aPD-1/CA + aPD-1 treatment, potentially contributing to improved immunotherapy outcomes.

### Heterogeneity and variation in stromal cells after treatment

Fibroblasts, the main stromal cells in the HGSC TME, were categorized and named into seven subtypes in this study (Fig. 7A). Inflammatory cancer-associated fibroblasts (iCAFs) express PDGFRα, CXCL12, and APOD and are enriched in detoxification processes and the TNF and IL-17 signaling pathways. Myofibroblastic CAFs (myCAFs) express smooth muscle-related genes (ACTA2 and POSTN) and are enriched in muscle contraction processes and pathways. iCAFs and myCAFs have also been identified in other cancers [45, 46]. Extracellular matrix-related CAFs (eCAFs) express IGFBP5 and PDGFRα and are involved in extracellular matrix-related processes. Antigen-presenting CAFs (apCAFs) express antigen-presenting genes (CD74 and HLA-DR) and are involved in antigen processing and presentation. Intermediate CAFs (inCAFs) are intermediate between iCAFs and myCAFs and express PDGFRα, CXCL12, COL11A1, and POSTN (Fig. 7B and C).

These cell types exhibit distinct differentiation levels and developmental trajectories. myCAFs are at the initial developmental stage, whereas iCAFs and eCAFs are present at all stages. apCAFs and fibroblasts are at the terminal stage (Fig. 7D and E). Although fibroblasts and apCAFs follow similar developmental paths, their differentiation levels differ significantly, indicating that their differentiation and developmental trajectories do not always correspond (Fig. 7F, S7A, S7B). Genes such as ACTB, ACTA2, TMSB4X, CD74, COX6C, OGN, and MYC may play roles in these transitions (Fig. S7C, S7D).

In the CA + PD-1 group, the proportion of fibroblasts increased, accompanied by a significant decrease in myCAFs (Fig. 7G and H). myCAFs promote tumor proliferation and invasion by secreting growth factors, cytokines, and enzymes that modify the microenvironment to support tumor growth and metastasis [47, 48]. This group also showed reduced enrichment in angiogenesis, EMT, hypoxia, and related oncogenic pathways, which was correlated with a decrease in EC8 cells and an increase in EC3 cells (Fig. 7I). Thus, the reduction in myCAFs might indicate a TME that is less conducive to tumor

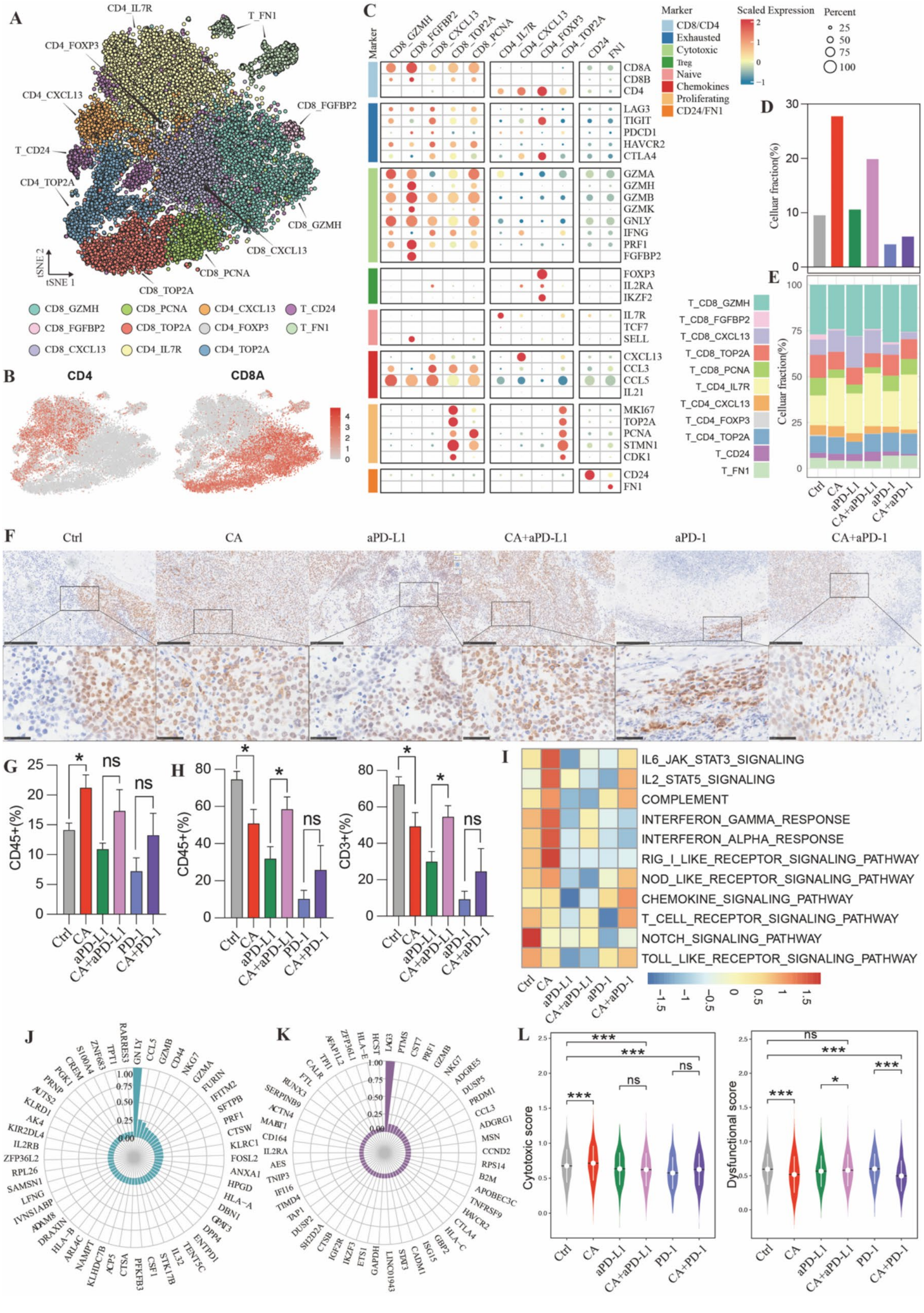

**Fig. 5** (See legend on next page.)

(See figure on previous page.)

**Fig. 5** Variation in T lymphocytes after different treatments in HGSC. (**A**) T-distributed stochastic neighbor embedding (t-SNE) visualization of T lymphocytes. (**B**) t-SNE showing the expression of CD8A and CD4 in T lymphocytes. (**C**) Expression of marker genes in different T lymphocyte subtypes. (**D**, **E**) Comparison of T lymphocytes and their subtypes among the different groups. (**F**) IHC results showing the changes in CD8 + T cells in the different groups. (**G**) CD45 + cell counts on day 14 of the experiment among the groups. (**H**) CD45 + and CD3 + cell counts on day 42 among the groups. (**I**) Immune-associated pathway enrichment analysis in different groups. (**J**, **K**) The top 50 genes correlated with GNLY and LAG3. (**L**) Comparison of CD8 T-cell cytotoxic scores and dysfunction scores among the groups

growth and survival. Different treatment groups also presented distinct regulon activities in fibroblasts (Fig. 7J). We also found more DEGs between the CA + aPD-1 and aPD-1 monotherapy groups than between the CA + aPD-L1 and aPD-L1 monotherapy groups (Fig. S7E). In the CA + aPD-1 group, genes such as APOD, OGN, FSTL1, IRFD1, and COL14A1 were upregulated, whereas SAA1 and CXCL12 were downregulated (Fig. S7F). Endothelial cells, another type of stromal cell in the TME, are classified into four subtypes (Fig. 7K and L). C1 has the lowest differentiation potential, whereas C3 has the highest (Fig. 7M). Following PD-1/CA + aPD-1 treatment, the proportion of C1 cells increased, whereas that of C2 cells decreased. Conversely, after PD-L1/CA + PD-L1 treatment, C2 levels increased, whereas C1 proportions decreased (Fig. 7N).

### Cell-to-cell communication analysis after treatment

To investigate changes in communication between tumor cells and other cell types posttreatment, we conducted cell−cell communication analysis. Compared with the control and monotherapy groups, the CA and combination treatment groups exhibited increased intercellular communication, especially between tumor cells and nontumor cells (Fig. 8A, S8A). These findings indicate that CA enhances interactions between tumor cells and other cell types.

Further analysis revealed APP-CD74 as the most critical ligand−receptor pair involved in communication between tumor cells and nontumor cell types (Fig. 8B). Additionally, essential ligand−receptor pairs involved in tumor cell communication with specific cell types, such as CD99/CD99 and HLA-A(B/C/E)-CD8A related to T cells, MDK-SDC4 (LRP1) related to fibroblasts and myeloid cells, and VEGFA(B)-VEGFR1 between tumor cells and endothelial cells, were identified. The communication between fibroblasts and tumor cells also involves ligand−receptor pairs such as COL1A1 (COL1A2)-SDC4 (Fig. 8B). In the corresponding communication pathways, the APP pathway, which exclusively includes APP-CD74, was present across all cell types (Fig. 8C and D, S8B), with CD74 widely expressed in various cells and APP expressed in all cells except T cells (Fig. 8E). In this pathway, tumor cells act as receivers, senders, and mediators, receiving APP signals from myeloid, fibroblast, and endothelial cells. Tumor cells also act on themselves and on T cells through autocrine and paracrine mechanisms (Figs. 8F, S8C). T cells receive signals only from other cell types, whereas myeloid cells, fibroblasts, and endothelial cells function solely as signal senders (Fig. 8F, S8C).

In addition to the APP signal, other critical pathways were identified. The COLLAGEN signaling pathway, which primarily includes the COL4A1 (COL1A1, COL2A2, and COL9A2)-SDC4 ligand−receptor pair, is found mainly between tumor cells, endothelial cells, and fibroblasts. T cells can also receive signals from endothelial cells, fibroblasts, and some tumor cells through this pathway. The MK signaling pathway, which consists of MDK-NCL (SDC4, SDC2, LRP1) ligand−receptor pairs, is present only between tumor cells and fibroblasts. The FN1 signaling pathway, which primarily includes FN1-SDC4 (ITGA5/ITGAV/ITGA3 + ITGB1), is unique in that among the tumor cell subtypes, only EC6 can emit this signal, which acts on all cells, with T cells serving solely as signal receivers. Additionally, the classical MHC-I pathway for T cells involves HLA-A (B/C/E/F)-CD8A pairs, where T cells remain as signal receivers, and the signal is primarily emitted by tumor cells. In contrast, in the CD99 pathway, both T cells and tumor cells can act as signal senders and receivers, suggesting more intimate and specific bidirectional communication between tumor cells and T cells through this pathway (Fig. S8B, S8C).

Finally, we compared changes in signaling pathways among the CA, combination treatment, control, and monotherapy groups. Compared with those in the control group, the APP, MK, CD99, and FN1 pathways were increased in the CA group and similarly increased in the CA + aPD-L1 group. In the CA + aPD-1 group, the APP pathway was weakened compared with that in the aPD-1 group, whereas the MK, CD99, and FN1 pathways were enhanced (Fig. 8G).

These findings suggest that CA enhances interactions between tumor cells and nontumor cells in the TME, which may contribute to the increased tumor-killing capacity of immunotherapy.

## Discussion

Immunotherapy has not met expectations in the treatment of HGSC because of the genetic complexity of the TME. Exploring the biological mechanisms of immune evasion and developing personalized therapeutic strategies are crucial. In this study, we successfully replicated the TME by generating PBMC-PDX models. To better understand the high heterogeneity of the intricate TME

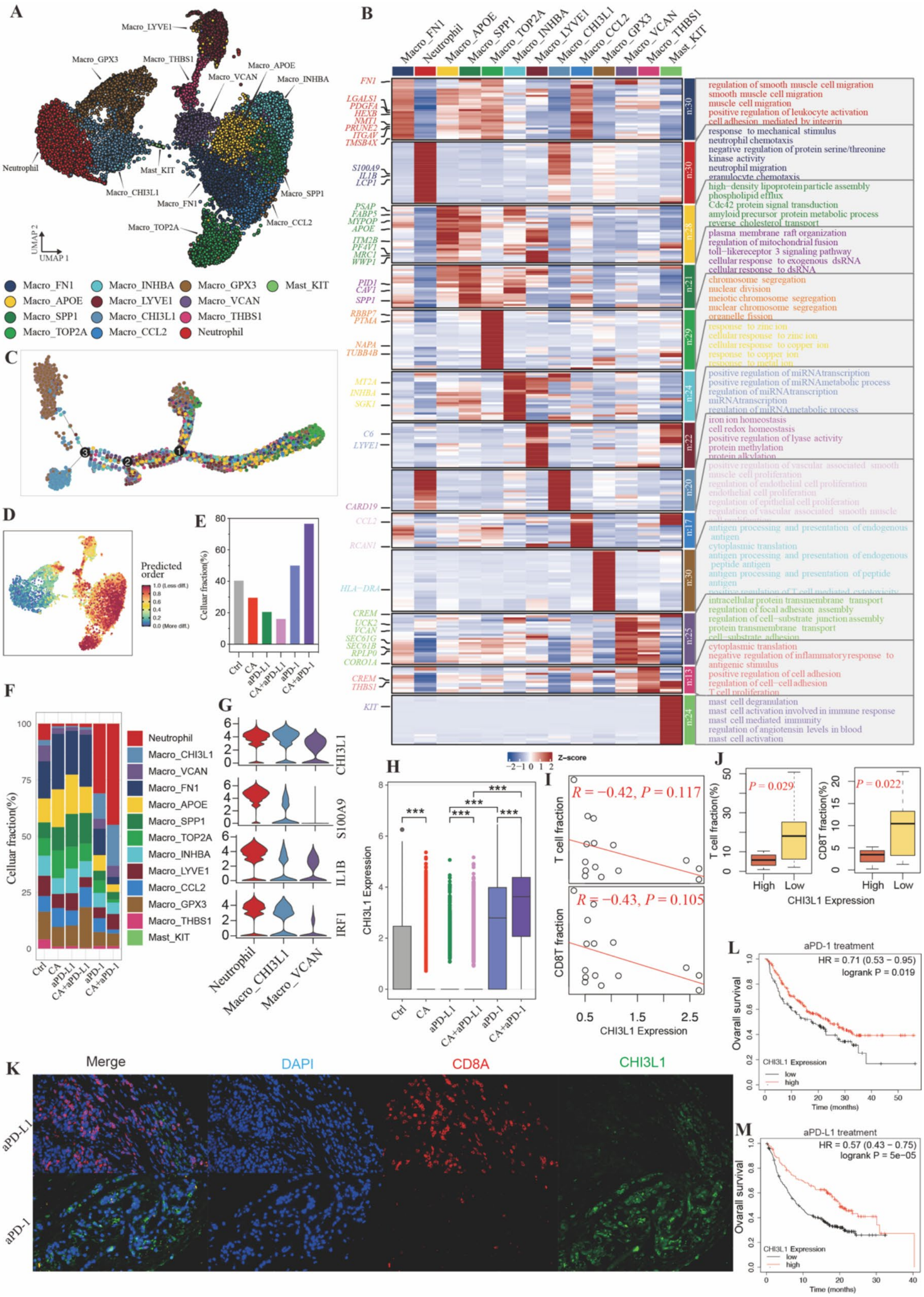

**Fig. 6** (See legend on next page.)

(See figure on previous page.)

**Fig. 6** Variation in myeloid cells after different treatments in HGSC. (**A**) UMAP visualization of myeloid cells. (**B**) The expression and associated biological processes of the top 30 marker genes in myeloid cell subtypes. (**C**) Pseudotime analysis of TAM subtypes. (**D**) Differential level analysis of myeloid cell subtypes. (**E**, **F**) Comparison of myeloid cells and their subtypes among different groups. (**G**) Violin plots showing the coexpressed genes in neutrophils, Macro-CHI3L1 and Macro-VCAN. (**H**) Expression of CHI3L1 in the different groups. (**I**) Correlations between T-cell and CD8 + T-cell fractions and CHI3L1 expression. (**J**) Comparison of high and low CHI3L1 expression in T-cell and CD8 + T-cell fractions. (**K**) Immunofluorescence image showing the relationship between CD8 T cells and CHI3L1 + cells. (**L**, **M**) Kaplan–Meier plot showing the correlation between CHI3L1 expression and overall survival (OS) in cancer patients treated with aPD-1/aPD-L1, with data sourced from the Kaplan–Meier Plotter database

and provide valuable insights into the design of effective strategies, we conducted scRNA-seq and identified various cell types in the TME, including tumor cells, myeloid cells, T lymphocytes, fibroblasts, endothelial cells, and their corresponding subtypes. These findings align with the cellular landscape of HGSC reported previously [22, 49].

Despite the substantial infiltration of CD8 + T cells observed in HGSC [50], previous clinical studies have reported unsatisfactory responses to PD-1 or PD-L1 blockade in patients with immunoreactive OC [51, 52]. Our study also suggested that aPD-L1 has no significant antitumor effect on HGSC, which is consistent with the findings of the IMagyn050 clinical trial [53]. In contrast, aPD-1 reduced both the tumor volume and the proportion of tumor cells, accompanied by variations in tumor cell subtypes and improvements in the immune suppression status of the TME. However, there were no evident signs of substantial changes in the status of CD8 + T cells after aPD-L1/aPD-1 treatment.

Additionally, we observed increased exchange of T lymphocytes between the peripheral blood and the TME after therapy, with lower levels of TILs and CD3 + cells in the aPD-1 group than in the control group, suggesting that T cells were recruited more after both treatments and consumed more T cells during aPD-1 treatment in the tumor cell-killing process. Considering the low expression of PD-L1 and PD-L2 in HGSC, we hypothesize that the differential effects between aPD-L1 and aPD-1 treatments may be attributed in part to the recruitment of new CD8 + T-cell clones from outside the tumor to replenish the TIL pool. To validate this, we sought methods to enhance this cellular exchange effect. CA, derived from the traditional folk medicine Echinacea purpurea, has been shown to have immune-enhancing and antitumor effects. Previous studies have reported that CA inhibits growth and promotes apoptosis in colon and gastric cancer cells [32, 33]. However, Cichello SA et al. reported that CA could exert a protumor effect on cervical cancer [54]. More importantly, CA promotes the proliferation of CD3+, CD4+, and CD8 + T cells [34]. In this study, we confirmed that CA does not have a significant antitumor effect when it acts directly on OV cells, which contradicts its reported tumor cell killing effects reported in other studies [32].

However, CA reduced the proportion of tumor cells accompanied by an increase in EC3 and a decrease in EC4 in the PBMC-PDX model, which we regarded as favorable indicators of tumor killing. This may be achieved by stimulating the proliferation of CD45 + and CD3 + cells and promoting the infiltration of lymphocytes into the TME, thus enhancing the tumor-killing ability of immune cells, similar to patients with greater CD8 + T-cell infiltration, who typically have better clinical outcomes [55, 56].

To verify whether CA could enhance the sensitivity of HGSC to immunotherapy, we treated HGSC with a combination of CA and aPD-L1/aPD-1 and found that both combinations had better treatment effects than did PD-L1/aPD-1 monotherapy, accompanied by higher percentages of CD45 + and CD3 + cells and TILs. Furthermore, we found that, compared with monotherapy, combination treatment increased immune responses in the TME, and the exhaustion score of CD8 + T cells in the CA + aPD-1 group was significantly lower than that in the monotherapy group. Therefore, we believe that although CA monotherapy results in changes in the state and quantity of CD8 + T cells, the enhanced antitumor effects of CA + aPD-1/aPD-L1 are due mainly to the increased quantity of TILs [57, 58]. The phenomenon of PBLs infiltrating the TME to supplement TILs has rarely been reported, possibly due to the dynamic nature of the process and the rapid replenishment of migrated PBLs, making detection challenging. Dev Bhatt et al. demonstrated that CD8 + TIL subsets share T-cell receptors with peripheral T cells via scRNA-seq [59]. Certain T lymphocytes in the TME, PB, and normal adjacent tissues undergo clonal expansion, and TILs in patients who respond to immunotherapy are replenished with fresh, unexhausted alternative cells from outside the tumor [60]. Another study suggested that chronic activation and exhaustion of preexisting TILs limit their reinvigoration following checkpoint inhibition and that the T-cell response to immunotherapy derives from a distinct repertoire of tumor-specific T-cell clones [61].

We also analyzed changes in other cell types and found that, compared with those in the PD-L1/CA + aPD-L1 group, the number of CHI3L1 + myeloid cells was significantly greater in the aPD-1/CA + aPD-1 group. CHI3L1 is expressed primarily in myeloid cells, especially neutrophils. We found that CHI3L1 could repel TILs and be detrimental to tumor prognosis, as reported in other studies [62–64]. However, CHI3L1 was recognized as a novel player in T-cell blockade in some reports [65]. A

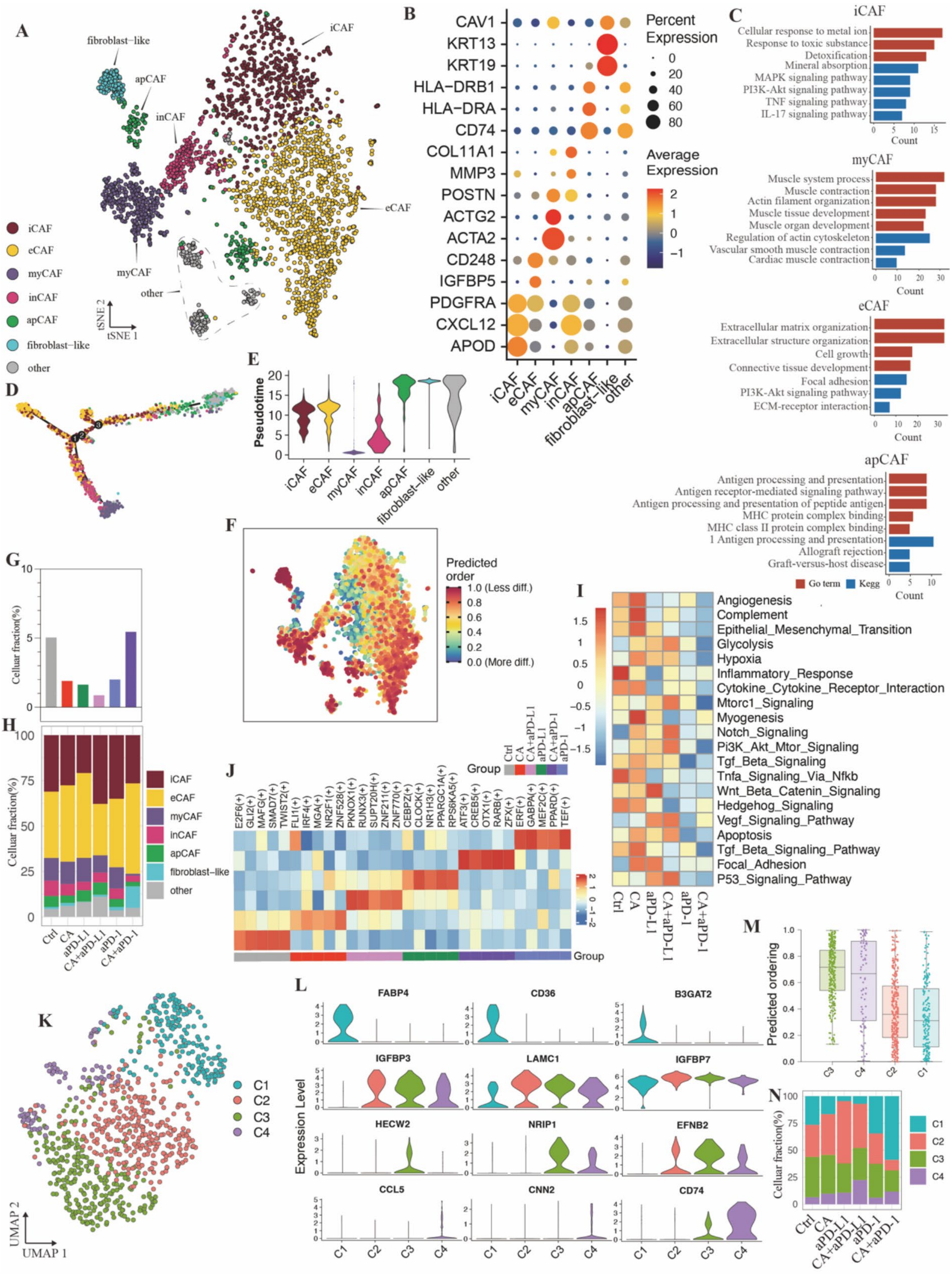

**Fig. 7** (See legend on next page.)

(See figure on previous page.)

**Fig. 7** Variation in stromal cells after different treatments in HGSC. (**A**) t-SNE visualization of fibroblasts. (**B**) Dot plot showing marker genes in fibroblast subtypes. (**C**) Gene Ontology (GO) analysis and Kyoto Encyclopedia of Genes and Genomes (KEGG) analysis of iCAFs, myCAFs, eCAFs, and apCAFs. (**D**, **E**) Pseudotime analysis of fibroblast subtypes. (**F**) Differential level analysis of fibroblast subtypes. (G, H) Comparison of fibroblasts and fibroblast subtypes among the different groups. (**I**) Pathway enrichment of fibroblasts after different treatments. (**J**) Top 5 activated transcription factor regulons of fibroblasts among the different groups. (**K**) UMAP visualization of endothelial cell subtypes. (**L**) Violin plot showing the expression levels of genes associated with endothelial cell subtypes. (**M**) Differentiation levels of endothelial cell subtypes. (**N**) Bar plot showing the percentages of endothelial cell subtypes in the different groups

clinical trial of aPD-1 in NSCLC reported that CHI3L1 was significantly overrepresented in the response group, with patients with higher CHI3L1 expression showing better PFS and OS and exhibiting better predictive ability than those with higher PD-L1 expression [66]. Another study showed that CHI3L1 can regulate the expression of PD-L1, PD-L2, and PD-1 and that targeting both CHI3L1 and PD-1 results in significantly enhanced antitumor responses [67]. Our study confirmed that CHI3L1 was associated with better immunotherapy outcomes, and the lower TILs in this group might result from the dual effects of tumor cell consumption and a greater proportion of CHI3L1 + cells. Moreover, considering that CHI3L1 can be secreted into intercellular spaces and peripheral blood [68–70], it may serve as a better potential marker for evaluating the immunotherapy effect in OC.

Finally, we found that both CA monotherapy and combination therapy increased intercellular communication between tumor cells and nontumor cells. APP-CD74 was identified as the most common ligand−receptor pair involved in communication between tumor and nontumor cells. APP-CD74 can influence tumor cells through paracrine mechanisms, affect tumor cells through paracrine signaling in myeloid and stromal cells, and act solely as a signal receiver in T cells. APP-CD74 has been found to participate in both autocrine and paracrine signaling in tumor cells and macrophages in kidney renal clear cell carcinoma [71]. It is also involved in neutrophil inhibition of T cells and interactions between B cells and M2 macrophages in gastric cancer [72, 73] and is significantly enriched and closely related to pancreatic cancer tumorigenesis [74]. Additionally, APP-CD74 influences the differentiation of immune cells and plays a crucial role in the immunotherapy response [75, 76]. However, few studies have elucidated the role of APP-CD74 in HGSC, indicating a need for further research.

In conclusion, our study comprehensively evaluated the therapeutic value of CA. The combination of CA and ICB demonstrated profound antitumor activity, with CA + aPD-1 showing the best effect, leading to significant tumor suppression and remarkable therapeutic efficacy in HGSC. CA may exert its effects through multiple mechanisms, including stimulating lymphocyte proliferation, promoting lymphocyte infiltration into the TME, altering lymphocyte states, enhancing inflammatory responses in the TME, and increasing interactions between tumor and nontumor cells. These discoveries provide new insights and directions for developing more effective immunotherapy strategies to improve the immunotherapy outcomes of OC patients.

While this study provides promising insights, several limitations remain. First, we used PBMC-PDX models derived from a single HGSC patient to evaluate the effects of CA combined with immunotherapy. Although this approach minimized inter-group variability, it also restricts the generalizability of our findings. To address this, we are currently constructing additional PDX models from other suitable HGSC patients to validate the broader applicability of our approach. Second, we used non-matched PBMCs for constructing the PBMC-PDX models. While this approach ensured a standardized, high-quality source of immune cells, it is may introduce variability in immune responses. Nevertheless, numerous studies have shown that PBMC-PDX models constructed with non-autologous PBMCs can still yield meaningful and reproducible results [77–79]. We are planning to incorporate patient-matched PBMCs whenever possible to more accurately replicate the tumor-immune microenvironment and improve the translational relevance of our models. Thirdly, the absence of direct confirmation of carboplatin and paclitaxel resistance in the PDX models is another limitation. Although the tumor samples were derived from chemo-resistant patients, we did not explicitly validate their resistance in these models. Lastly, although this study provides a relatively comprehensive evaluation of CA's immunotherapy-enhancing effects as exploratory research, it lacks sufficient experiments, such as fluorescence-labeled cell-tracking techniques, to further validate T lymphocyte migration. We plan to conduct in-depth studies on the functional mechanisms to elucidate the precise ways in which CA exerts its immunomodulatory activity.

## Conclusions

In this study, we found that CA not only increased the antitumor activity of immune cells but also promoted the infiltration of T cells into the TME. We further demonstrated that combining CA with PD-1/PD-L1 blockade significantly improved the response of OC patients to ICB immunotherapy. This combination could be a promising therapeutic strategy for improving outcomes in OC patients.

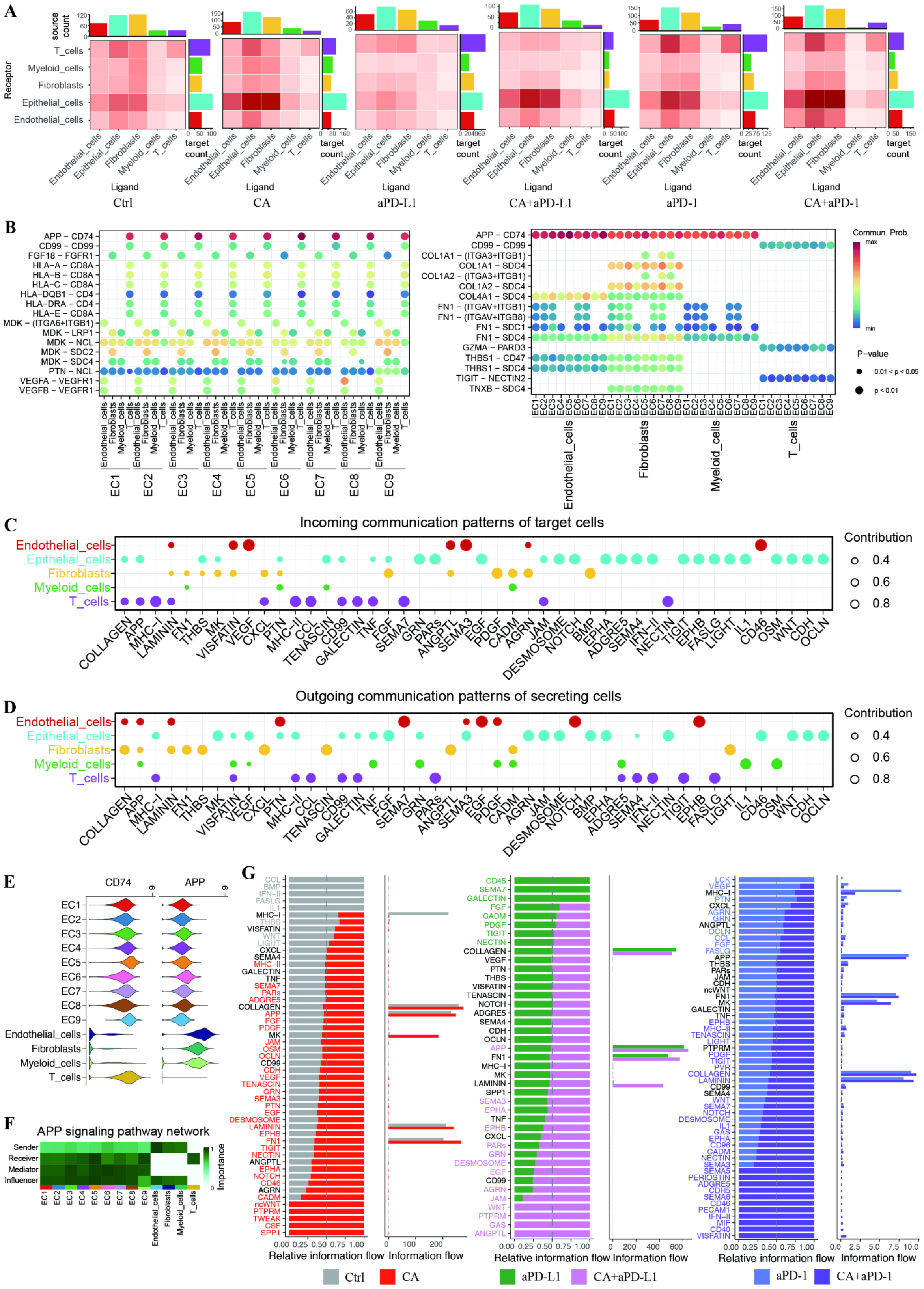

**Fig. 8** (See legend on next page.)

(See figure on previous page.)

**Fig. 8** Cell-cell communication between tumor cells and other cell types. (**A**) Heatmap showing the number of total potential ligand–receptor pairs between different cell types in each group obtained with CellChat. The bar plot represents the sum of a column or row. (**B**) Dot plot showing the main significant ligand–receptor pairs between tumor cell subtypes and nontumor cells. The dot color and size represent the calculated communication probability and *p* value, respectively. *p* values are computed from a one-sided permutation test. (**C**, **D**) Dot plot showing the incoming and outgoing signaling networks of secreted cells in different cell types. (**E**) Violin plot showing the expression distribution of signaling genes involved in the inferred APP signaling network. (**F**) Heatmap showing the relative importance of different cell types on the basis of the four computed network centrality measures of the APP signaling network. (**G**) Bar plots of signaling axes ranked according to overall information flow differences in interaction networks between the control and CA groups and between the aPD-1/aPD-L1 and CA + aPD-1/aPD-L1 groups

## Methods

### Preparation and processing of the HGSC samples

After obtaining the patient's consent and approval from the Ethics Committee of Qingdao University Affiliated Hospital, we obtained 700 ml of malignant ascites from a 47-year-old female patient diagnosed with advanced HGSC (accompanied by metastases to the liver, peritoneum, pelvis, and multiple lymph nodes). Previously, the patient underwent tumor debulking surgery followed by ten cycles of postoperative adjuvant chemotherapy with paclitaxel + carboplatin. Additionally, seven cycles of paclitaxel liposomes + cisplatin and two cycles of sequential treatment with pemetrexed + cisplatin + bevacizumab were administered. However, after these treatments, the patient's tumor increased in size, and there was an increase in abdominal ascites, leading to the diagnosis of progressive disease (PD). Genetic testing revealed TP53 mutation, MYC amplification, low tumor mutation burden (7.1 muts/Mb), microsatellite stability (MSS), and low PD-L1 (22C3) expression (TPS < 1%). No BRCA1/2 mutation was detected.

### Construction of the PDX model

The ascites sample was transferred to a biosafety cabinet and centrifuged in a 50 mL centrifuge tube (500 × g, 5 min). The supernatant was discarded, RBC lysis buffer was added, and the mixture was incubated at room temperature for 5 min to lyse the red blood cells. PBS was added, and the mixture was mixed well and centrifuged at 1200 rpm for 3 min. The supernatant was discarded, and the tumor cells were enriched. The tumor cells were washed twice with PBS and centrifuged to remove the supernatant, the tumor cells were resuspended in precooled PBS, and the matrix gel was added at a 1:1 volume ratio. The tumor cells were subcutaneously injected into NSG mice. The health status of the mice was observed daily, and the tumor volume was measured periodically. The tumor volume was calculated as V = 0.5* length * width2. When the tumor grew to an appropriate size, part of the tumor was removed for pathological examination, frozen and stored, and this generation was referred to as the P0 generation. After a pathologist confirmed that the pathological type of the model tumor was the same as that of the original tumor, the tumor was allowed to grow in NSG mice.

### Construction of the PBMC-PDX model

PBMCs were purchased from Miaoshun Biotechnology Co. (Shanghai, China) and were thawed as follows: heated in a water bath at 37 °C, washed with PBS buffer, centrifuged (400 g, 10 min), resuspended in PBS buffer, and counted, after which the cell concentration was adjusted to 2.5*107/ml. Previously obtained tumor tissues were evenly cut into approximately 3 mm*3 mm*3 mm tissue blocks and then implanted subcutaneously on the right dorsal side of each NSG mouse as described above. After the average tumor volume reached approximately 150–250 mm3, PBMCs were injected into the PDX model mice at a dose of 0.2 ml (5*106 cells/mouse). Fluorescence-activated cell sorting (FACS) was used to evaluate the successful construction of the PBMC-PDX model, and the same steps were then followed to continue the construction of the PBMC-PDX model for drug efficacy testing.

### Drugs

The PD-L1-specific antibody atezolizumab (1200 mg/20 mL) was purchased from Roche (Basel, Switzerland). The PD-1-specific antibody toripalimab (240 mg/5 mL) was purchased from Suzhou Zhenhe Biomedical Pharmaceutical Co. (Suzhou, China). CA was purchased from Sigma Chemical Co. (St. Louis, MO, USA). For the cell experiments, CA was first dissolved in DMSO to prepare a 100 mM solution, diluted with cell culture medium to final concentrations of 10 μM, 50 μM, and 100 μM, and then added to different treatment groups. The use of CA in the animal experiment is detailed in Supplementary 1.

### Animal experiments

Female NSG mice, aged 6–8 weeks and weighing approximately 18–20 g, were purchased from Shanghai Model Organisms Center, Inc. (certificate number: 20170010009719; Shanghai, China). All the mice were housed in an SPF level animal room with an IVC constant temperature and humidity system, with a temperature of 20–26 °C, a humidity level of 40–70%, and a light cycle of 12 h light and 12 h dark. Three NSG mice were housed in each cage measuring 325 mm × 210 mm × 180 mm, and the bedding used in the cages was a corn cob that was sterilized by high pressure and changed twice a week. Throughout the experiment, all the mice had free access to food and water. The feed was sterilized by Co60 irradiation, and the drinking water was sterilized by high pressure and changed twice a week. The tumor-bearing mice were euthanized when they became extremely emaciated and were nearly dead or when the average tumor volume reached 2000 mm3. At the end of the experiment, all the mice were euthanized. The animal protocol was approved by the Institutional Animal Care and Use Committee.

### Cell counting Kit-8 (CCK-8) assay

The OC cell line SKOV-3 was treated with CA (0, 10, 50, or 100 μM), PBMCs, or a combination of CA and PBMCs for cell experiments. SKOV-3 cells were seeded into a 96-well plate at a density of 1 × 104 cells per well and incubated to allow attachment. Ten microliters of CCK-8 solution were added to each well, and the plate was incubated for 2–4 h. The absorbance at 450 nm was measured via a microplate reader. The relative cell viability or proliferation rate was calculated by comparing the absorbance of the treated wells to that of the control wells. A CCK-8 assay kit was purchased from TargetMol Chemicals (MA, USA).

### Annexin V-FITC assay

The treated SKOV-3 cell culture medium was aspirated into a centrifuge tube. The adherent cells were washed with PBS, and an appropriate amount of trypsin digestion solution (without EDTA) was added to digest the cells. The mixture was incubated at room temperature until the cells were gently dislodged by tapping. The cell culture medium collected in the first step was added to neutralize the trypsin, and the already suspended apoptotic or necrotic cells were collected. The cells were transferred to a centrifuge tube and centrifuged at 400 × g for 5 min. The supernatant was discarded, the cells were gently resuspended in PBS, and the cells were counted. A total of 1 × 105 resuspended cells were centrifuged at 400 × g for 5 min at 4 °C, the supernatant was discarded, and the cells were gently resuspended in 195 μl of Annexin V-FITC binding buffer. Next, 5 μl of Annexin V-FITC was added, and the mixture was mixed gently, followed by the addition of 10 μl of propidium iodide (PI) staining solution. The mixture was incubated at room temperature (20–25 °C) in the dark for 20 min. Then, flow cytometry detection was performed. An Annexin V-FITC apoptosis detection kit was purchased from Beyotime Biotechnology (Shanghai, China).

### Fluorescence-activated cell sorting (FACS)

FACS was performed via an Attune® NxT Acoustic Focusing Cytometer (Life Technologies, CA, USA). The following antibodies were used: APC-conjugated anti-human CD45, APC/Cy7-conjugated anti-human CD8, PE-conjugated anti-human CD3, PE-conjugated anti-human CD56 from Biolegend (CA, USA), and BV421-conjugated anti-human CD45, BB515-conjugated anti-human CD3, and BV605-conjugated anti-human CD4 from BD (NJ, USA).

To evaluate the PBMC-PDX model, peripheral blood was collected from the PDX model mice, mixed with 1 mL of lysis buffer per tube, and incubated at room temperature in the dark for 10 min to lyse red blood cells, followed by centrifugation at 300 × g for 5 min at 4 °C. The supernatant was collected and washed twice with staining buffer, and a small amount of human PBMCs was added, mixed and divided into 4 tubes (100 μL in each tube). The tubes were treated as follows: (1) Blank, (2) For CD45 single staining, 5 μL of anti-human CD45 antibody was added. (3) For CD3 single staining, 5 μL of anti-human CD3 antibody was added, and (4) Then, 5 μL of CD45 antibody and 5 μL of CD3 antibody were added to the mixture. After this, the tubes were incubated in the dark at 4 °C for 30 min. The cells were washed twice with staining buffer, centrifuged at 400 × g for 5 min, and resuspended in 200 μL of staining buffer before analysis. The gating strategy was set as follows: R1, total cells; R2, single cells; and R3, CD45 + CD3 + cells.

To compare the therapeutic effects of the treatments, the treated peripheral blood of the PBMC-PDX model mice was mixed and divided into seven tubes, each containing 100 μL. The tubes were treated as follows: (1) Blank, (2) For CD45 single staining, 5 μL of anti-human CD45 antibody was added. (3) For CD3 single staining, 5 μL of anti-human CD3 antibody was added. (4) For CD4 single staining, 5 μL of anti-human CD4 antibody was added. (5) For CD8 single staining, 5 μL of anti-human CD8 antibody was added. (6) For CD56 single staining, 5 μL of anti-human CD56 antibody was added, and (7) The following mixtures were used: 5 μL of CD45 antibody, 5 μL of CD3 antibody, 5 μL of CD4 antibody, 5 μL of CD8 antibody, and 5 μL of CD56 antibody. The gating strategy was set as follows: R1: total cells, R2: single cells, R3: CD45 + cells, R4: CD45 + CD3 + cells, R5: CD4 + cells, R6: CD8 + cells, and R7: CD45 + CD56 + cells.

### Single-cell RNA sequencing and analysis

A total of 15 samples were collected from the PBMC-PDX model mice, with 3 samples from the control group, 4 samples from the CA treatment group, and the remaining 8 samples from the aPD-L1, aPD-1, CA + aPD-L1, and CA + aPD-1 treatment groups (2 samples per group). The collected tumor tissue was cut into 1–2 mm3 pieces and digested with a SoloTM Tumor Dissociation Kit (Sinotech Genomics, JZ-SC-58201) for 60 min at 37 °C. A 40 μm cell strainer-filtered single-cell mixture was kept on ice until single-cell transcriptome analysis was performed after the digestion was stopped with RPMI-1640.

Single-cell transcriptome analysis was conducted in strict accordance with the protocol of the BD Rhapsody system (BD Biosciences, CA). First, the cells were stained with calcein AM and Draq7 for precise determination of the cell concentration and viability via a BD Rhapsody™ Scanner and loaded in a microwell cartridge. The cell capture beads were then loaded onto the cartridge excessively, and the cell capture beads were further retrieved and washed prior to performing reverse transcription after lysing the cells with lysis buffer.

The cDNA library containing the cell labels and UMI information was finally prepared on the basis of the microbead-captured single-cell transcriptome via a BD Rhapsody cDNA Kit (BD Biosciences, Cat. No. 633773) and a BD RhapsodyTM WTA Amplification Kit (BD Biosciences, Cat. No. 633801). All libraries were sequenced in PE150 mode (paired-end 150 bp reads) on the NovaSeq platform. The raw reads were processed to generate a single-cell expression matrix through the BD Rhapsody Whole Transcriptome Assay Analysis Pipeline (v1.8), which includes filtering by read quality, annotation of reads and molecules, and determination of putative cells. The Genome Reference Consortium Human Build 38 (GRCh38) was used as a reference for the BD pipeline.

R software (v4.2.0) [80] and the Seurat R package (v4.3.0) [81] were used for subsequent clustering analysis and visualization. Cells with more than 25% mitochondrial UMI, less than 500 UMI or 200 genes were excluded. The gene expression matrix was then normalized to the total cellular UMI count, and 2000 highly variable features were selected for PCA after scaling the data with respect to UMI counts. In addition, the first 50 principal components were further chosen for clustering at a resolution of 0.6 via either t-distributed stochastic neighbor embedding (t-SNE) or the uniform manifold approximation and projection (UMAP) algorithm. Feature plots, violin plots and heatmaps were used to visualize the expression of the indicated genes in each cluster.

Specific markers for each cluster were identified via the FindAllMarkers function with the Wilcoxon test under the following criteria: log2-fold change > 0.25; min.pct > 0.25. To identify the cell type in the filtered sample datasets and the combined dataset in an unbiased manner, we annotated the cell type for each cluster with the SingleR R package (v1.4.1) [82] and canonical marker genes reported previously. The ClusterProfiler R package (v4.4.4) [83] was used for Gene Ontology (GO) and Kyoto Encyclopedia of Genes and Genomes (KEGG) functional enrichment analysis. The GSVA [84] and msigdbr [85] R packages were used for hallmark and KEGG pathway enrichment analysis. The SCENIC package [86] was employed for transcription factor analysis, whereas CellChat [87] was utilized for cell−cell communication analysis. Pseudotime trajectory analysis of cell types was conducted via the Monocle2 R package (v2.18.0) [88] with the DDR-Tree reduction method.

### Hematoxylin and eosin (H&E) staining, immunohistochemistry (IHC) and IF

The tumor tissues were fixed in 4% paraformaldehyde, dehydrated via an ethanol gradient (70%, 85%, 95%, 100%), embedded in paraffin, cut into 5 µm-thick sections via a paraffin-embedded tissue microtome (RM2235, Leica, Wetzlar, Germany) and dried in an oven (DZF-6050, Blue Pard, Shanghai, China) at 60 °C for 2 h. The pathological sections were then deparaffinized in xylene, rehydrated in a gradient of ethanol (100%, 95%, 85%, 70%) and washed with phosphate-buffered saline (P3813-10PAK, Sigma, USA).

For HE staining, the sections were immersed in hematoxylin solution for 5 min and then added to eosin solution (BA4024, Baso, Zhuhai, China) for 3 min, followed by microscopic examination. The sections were dehydrated and mounted.

For IHC, antigen retrieval was performed using Tris-EDTA buffer (95 °C, 20 min), and the samples were cooled in a water bath for 5 min. Rabbit anti-human CD8 alpha (ab205921, 1:1000 dilution; Abcam, Cambridge, UK) or rabbit anti-human PD-L1 (PA5-28115, 1:800 dilution; Invitrogen, USA) was added. The next steps were performed via the Mouse and Rabbit Specific HRP/DAB IHC Detection Kit-Micropolymer (ab236466; Abcam, Cambridge, UK) according to the manufacturer's instructions. The rabbit (DA1E) mAb IgG XP® isotype control (#3900, Cell Signaling, Danvers, MA, USA) was used as a negative control for IHC.

For IF, first, the slides were incubated at 60 °C for 2 h. Then, the slides were sequentially immersed in xylene, anhydrous ethanol, 95% ethanol, 85% ethanol, 75% ethanol, and ddH2O for 10 min each for deparaffinization. The samples were subjected to antigen retrieval via sodium citrate antigen retrieval solution at 95 °C for 30 min and then cooled to room temperature. After the samples were washed with PBS, an endogenous peroxidase blocker was used for 20 min. After another PBS wash, the slides were blocked with 10% goat serum at room temperature for 30 min. The samples were blotted dry without washing, and then, the following primary antibodies were added: rabbit anti-human CD8 alpha (ab316778, 1:200 dilution; Abcam, UK) and mouse anti-human CHI3L1 (sc-393494, 1:100 dilution; Santa Cruz, USA). The samples were incubated overnight at 4 °C. After washing with PBS, the slides were incubated with fluorescent secondary antibodies (rabbit anti-Alexa Fluor 594, red fluorescence; mouse anti-Alexa Fluor 488, green fluorescence; each diluted 1:200, Abcam, UK) at room temperature for 1 h. The nuclei were subsequently counterstained with DAPI (ab104139, Cambridge, UK) for blue fluorescence. The stained slides were observed under a fluorescence microscope.

### Statistical analysis

All the data are presented as the means ± SEMs. The Mann–Whitney test or Student's t test was used to compare the differences between different groups. Data analysis and visualization were performed via the GraphPad Prism 9, R, and R packages. The statistical significance was set at $P < 0.05$. The tumor growth inhibition rate (TGI%) was calculated as [1-T/C] × 100.

## Supplementary Information

The online version contains supplementary material available at https://doi.org/10.1186/s12964-025-02146-7.

Supplementary Material 1

**Acknowledgements**

This manuscript is part of the doctoral thesis of H.L.

### Author contributions

XZ, NZ and HL designed the study. HL conducted the experiments, performed the bioinformatics analysis, and wrote the manuscript. JZ and HH ¬collected the biospecimens. XH and CZ were involved in constructing the PBMC-PDX model. YZ and FY were involved in performing hematoxylin and eosin (H&E) staining and immunohistochemistry. All the authors read and approved the final manuscript.

**Funding**

This work was supported by a grant from the project ZR2022MH048 supported by the Shandong Provincial Natural Science Foundation (Xiaochun Zhang), the National Natural Science Foundation of China (82272693 to Na Zhou), and the Qilu Health Leading Talents Training Project (Na Zhou).

### Data availability

Data is provided within the manuscript or supplementary information files.

## Declarations

### Ethics approval and consent to participate

This study was conducted in accordance with the Declaration of Helsinki and received full approval from the Medical Ethics Review Committee of the Affiliated Hospital of Qingdao University (QYFYWZLL27943).

### Consent for publication

Not applicable.

### Competing interests

The authors declare no competing interests.

### Author agreement

All the authors have reviewed and approved the final version of the manuscript being submitted.

**Author details**

[1]Precision Medicine Center of Oncology, The Affiliated Hospital of Qingdao University, No. 56 Haier Road, Qingdao 266000, Shandong, China
[2]Department of Oncology, The Affiliated Hospital of Qingdao University, No. 7 Jiaxing Road, Qingdao 266000, Shandong, China

Received: 16 December 2024 / Accepted: 8 March 2025

### References

1. Matulonis UA, Sood AK, Fallowfield L, Howitt BE, Sehouli J, Karlan BY. Ovarian cancer. Nat Rev Dis Primers. 2016;2:16061.
2. Sung H, Ferlay J, Siegel RL, Laversanne M, Soerjomataram I, Jemal A, Bray F. Global cancer statistics 2020: GLOBOCAN estimates of incidence and mortality worldwide for 36 cancers in 185 countries. CA Cancer J Clin. 2021;71:209–49.
3. Ghisoni E, Imbimbo M, Zimmermann S, Valabrega G. Ovarian cancer immunotherapy: turning up the heat. Int J Mol Sci 2019, 20.
4. Ghoneum A, Almousa S, Warren B, Abdulfattah AY, Shu J, Abouelfadl H, Gonzalez D, Livingston C, Said N. Exploring the clinical value of tumor microenvironment in platinum-resistant ovarian cancer. Semin Cancer Biol. 2021;77:83–98.
5. Xu J, Fang Y, Chen K, Li S, Tang S, Ren Y, Cen Y, Fei W, Zhang B, Shen Y, Lu W. Single-Cell RNA sequencing reveals the tissue architecture in human High-Grade serous ovarian cancer. Clin Cancer Res. 2022;28:3590–602.
6. Kandalaft LE, Odunsi K, Coukos G. Immunotherapy in ovarian cancer: are we there yet?? J Clin Oncol. 2019;37:2460–71.
7. Alexandrov LB, Nik-Zainal S, Wedge DC, Aparicio SA, Behjati S, Biankin AV, Bignell GR, Bolli N, Borg A, Børresen-Dale AL, et al. Signatures of mutational processes in human cancer. Nature. 2013;500:415–21.
8. Zhou N, Jiang M, Zhang X. Benefits of precision medicine in lung cancer: experience from a single institution. Vis Cancer Med. 2022;3:4.
9. Iyer S, Zhang S, Yucel S, Horn H, Smith SG, Reinhardt F, Hoefsmit E, Assatova B, Casado J, Meinsohn MC, et al. Genetically defined syngeneic mouse models of ovarian cancer as tools for the discovery of combination immunotherapy. Cancer Discov. 2021;11:384–407.
10. Duan Q, Zhang H, Zheng J, Zhang L. Turning cold into hot: firing up the tumor microenvironment. Trends Cancer. 2020;6:605–18.
11. Invrea F, Rovito R, Torchiaro E, Petti C, Isella C, Medico E. Patient-derived xenografts (PDXs) as model systems for human cancer. Curr Opin Biotechnol. 2020;63:151–6.
12. Yoshida GJ. Applications of patient-derived tumor xenograft models and tumor organoids. J Hematol Oncol. 2020;13:4.
13. Karkampouna S, La Manna F, Benjak A, Kiener M, De Menna M, Zoni E, Grosjean J, Klima I, Garofoli A, Bolis M, et al. Patient-derived xenografts and organoids model therapy response in prostate cancer. Nat Commun. 2021;12:1117.
14. Lee HW, Chung W, Lee HO, Jeong DE, Jo A, Lim JE, Hong JH, Nam DH, Jeong BC, Park SH, et al. Single-cell RNA sequencing reveals the tumor microenvironment and facilitates strategic choices to circumvent treatment failure in a chemorefractory bladder cancer patient. Genome Med. 2020;12:47.
15. Sun H, Cao S, Mashl RJ, Mo CK, Zaccaria S, Wendl MC, Davies SR, Bailey MH, Primeau TM, Hoog J, et al. Comprehensive characterization of 536 patient-derived xenograft models prioritizes candidatesfor targeted treatment. Nat Commun. 2021;12:5086.
16. Teng S, Li YE, Yang M, Qi R, Huang Y, Wang Q, Zhang Y, Chen S, Li S, Lin K, et al. Tissue-specific transcription reprogramming promotes liver metastasis of colorectal cancer. Cell Res. 2020;30:34–49.
17. Liu JF, Palakurthi S, Zeng Q, Zhou S, Ivanova E, Huang W, Zervantonakis IK, Selfors LM, Shen Y, Pritchard CC, et al. Establishment of Patient-Derived tumor xenograft models of epithelial ovarian cancer for preclinical evaluation of novel therapeutics. Clin Cancer Res. 2017;23:1263–73.
18. Kim H, George E, Ragland R, Rafail S, Zhang R, Krepler C, Morgan M, Herlyn M, Brown E, Simpkins F. Targeting the ATR/CHK1 axis with PARP Inhibition results in tumor regression in BRCA-Mutant ovarian cancer models. Clin Cancer Res. 2017;23:3097–108.
19. George E, Kim H, Krepler C, Wenz B, Makvandi M, Tanyi JL, Brown E, Zhang R, Brafford P, Jean S, et al. A patient-derived-xenograft platform to study BRCA-deficient ovarian cancers. JCI Insight. 2017;2:e89760.
20. Kondrashova O, Topp M, Nesic K, Lieschke E, Ho GY, Harrell MI, Zapparoli GV, Hadley A, Holian R, Boehm E, et al. Methylation of all BRCA1 copies predicts response to the PARP inhibitor Rucaparib in ovarian carcinoma. Nat Commun. 2018;9:3970.
21. Dong R, Qiang W, Guo H, Xu X, Kim JJ, Mazar A, Kong B, Wei JJ. Histologic and molecular analysis of patient derived xenografts of high-grade serous ovarian carcinoma. J Hematol Oncol. 2016;9:92.
22. Izar B, Tirosh I, Stover EH, Wakiro I, Cuoco MS, Alter I, Rodman C, Leeson R, Su MJ, Shah P, et al. A single-cell landscape of high-grade serous ovarian cancer. Nat Med. 2020;26:1271–9.
23. Olalekan S, Xie B, Back R, Eckart H, Basu A. Characterizing the tumor microenvironment of metastatic ovarian cancer by single-cell transcriptomics. Cell Rep. 2021;35:109165.

24. Laumont CM, Wouters MCA, Smazynski J, Gierc NS, Chavez EA, Chong LC, Thornton S, Milne K, Webb JR, Steidl C, Nelson BH. Single-cell profiles and prognostic impact of Tumor-Infiltrating lymphocytes coexpressing CD39, CD103, and PD-1 in ovarian cancer. Clin Cancer Res. 2021;27:4089–100.
25. Olbrecht S, Busschaert P, Qian J, Vanderstichele A, Loverix L, Van Gorp T, Van Nieuwenhuysen E, Han S, Van den Broeck A, Coosemans A, et al. High-grade serous tubo-ovarian cancer refined with single-cell RNA sequencing: specific cell subtypes influence survival and determine molecular subtype classification. Genome Med. 2021;13:111.
26. Launonen IM, Lyytikäinen N, Casado J, Anttila EA, Szabó A, Haltia UM, Jacobson CA, Lin JR, Maliga Z, Howitt BE, et al. Single-cell tumor-immune microenvironment of BRCA1/2 mutated high-grade serous ovarian cancer. Nat Commun. 2022;13:835.
27. Fu R, Zhang P, Jin G, Wang L, Qi S, Cao Y, Martin C, Zhang Y. Versatility in acyltransferase activity completes Chicoric acid biosynthesis in purple Coneflower. Nat Commun. 2021;12:1563.
28. Lee J, Scagel CF. Chicoric acid: chemistry, distribution, and production. Front Chem. 2013;1:40.
29. Fu R, Zhang P, Deng Z, Jin G, Zhang Y. Chicoric acid provides better ultraviolet protection than the sum of its substrates in purple Coneflower plants. Ind Crops Prod 2021:170.
30. Dy GK, Bekele L, Hanson LJ, Furth A, Mandrekar S, Sloan JA, Adjei AA. Complementary and alternative medicine use by patients enrolled onto phase I clinical trials. J Clin Oncol. 2004;22:4810–5.
31. Werneke U, Earl J, Seydel C, Horn O, Crichton P, Fannon D. Potential health risks of complementary alternative medicines in cancer patients. Br J Cancer. 2004;90:408–13.
32. Sun X, Zhang X, Zhai H, Zhang D, Ma S. Chicoric acid (CA) induces autophagy in gastric cancer through promoting Endoplasmic reticulum (ER) stress regulated by AMPK. Biomed Pharmacother. 2019;118:109144.
33. Tsai YL, Chiu CC, Yi-Fu Chen J, Chan KC, Lin SD. Cytotoxic effects of Echinacea purpurea flower extracts and cichoric acid on human colon cancer cells through induction of apoptosis. J Ethnopharmacol. 2012;143:914–9.
34. Kour K, Bani S. Augmentation of immune response by Chicoric acid through the modulation of CD28/CTLA-4 and Th1 pathway in chronically stressed mice. Neuropharmacology. 2011;60:852–60.
35. Park SJ, Lee M, Kim D, Oh DH, Prasad KS, Eun S, Lee J. Echinacea purpurea extract enhances natural killer cell activity in vivo by upregulating MHC II and Th1-type CD4(+) T cell responses. J Med Food. 2021;24:1039–49.
36. Dijkstra KK, Cattaneo CM, Weeber F, Chalabi M, van de Haar J, Fanchi LF, Slagter M, van der Velden DL, Kaing S, Kelderman S, et al. Generation of tumor-Reactive T cells by Co-culture of peripheral blood lymphocytes and tumor organoids. Cell. 2018;174:1586.e15981512.
37. Donato C, Kunz L, Castro-Giner F, Paasinen-Sohns A, Strittmatter K, Szczerba BM, Scherrer R, Di Maggio N, Heusermann W, Biehlmaier O, et al. Hypoxia triggers the intravasation of clustered Circulating tumor cells. Cell Rep. 2020;32:108105.
38. Gilkes DM, Semenza GL, Wirtz D. Hypoxia and the extracellular matrix: drivers of tumour metastasis. Nat Rev Cancer. 2014;14:430–9.
39. Liu J, Huang Z, Chen HN, Qin S, Chen Y, Jiang J, Zhang Z, Luo M, Ye Q, Xie N, et al. ZNF37A promotes tumor metastasis through transcriptional control of THSD4/TGF-β axis in colorectal cancer. Oncogene. 2021;40:3394–407.
40. Riffle S, Hegde RS. Modeling tumor cell adaptations to hypoxia in multicellular tumor spheroids. J Exp Clin Cancer Res. 2017;36:102.
41. Jing X, Yang F, Shao C, Wei K, Xie M, Shen H, Shu Y. Role of hypoxia in cancer therapy by regulating the tumor microenvironment. Mol Cancer. 2019;18:157.
42. Tang Z, Kang B, Li C, Chen T, Zhang Z. GEPIA2: an enhanced web server for large-scale expression profiling and interactive analysis. Nucleic Acids Res. 2019;47:W556–60.
43. Li T, Fu J, Zeng Z, Cohen D, Li J, Chen Q, Li B, Liu XS. TIMER2.0 for analysis of tumor-infiltrating immune cells. Nucleic Acids Res. 2020;48:W509–14.
44. Győrffy B. Integrated analysis of public datasets for the discovery and validation of survival-associated genes in solid tumors. Innov (Camb). 2024;5:100625.
45. Hutton C, Heider F, Blanco-Gomez A, Banyard A, Kononov A, Zhang X, Karim S, Paulus-Hock V, Watt D, Steele N, et al. Single-cell analysis defines a pancreatic fibroblast lineage that supports anti-tumor immunity. Cancer Cell. 2021;39:1227–e12441220.
46. Kieffer Y, Hocine HR, Gentric G, Pelon F, Bernard C, Bourachot B, Lameiras S, Albergante L, Bonneau C, Guyard A, et al. Single-Cell analysis reveals fibroblast clusters linked to immunotherapy resistance in cancer. Cancer Discov. 2020;10:1330–51.
47. Chen C, Guo Q, Liu Y, Hou Q, Liao M, Guo Y, Zang Y, Wang F, Liu H, Luan X, et al. Single-cell and Spatial transcriptomics reveal POSTN(+) cancer-associated fibroblasts correlated with immune suppression and tumour progression in non-small cell lung cancer. Clin Transl Med. 2023;13:e1515.
48. Lin SC, Liao YC, Chen PM, Yang YY, Wang YH, Tung SL, Chuang CM, Sung YW, Jang TH, Chuang SE, Wang LH. Periostin promotes ovarian cancer metastasis by enhancing M2 macrophages and cancer-associated fibroblasts via integrin-mediated NF-κB and TGF-β2 signaling. J Biomed Sci. 2022;29:109.
49. Hornburg M, Desbois M, Lu S, Guan Y, Lo AA, Kaufman S, Elrod A, Lotstein A, DesRochers TM, Munoz-Rodriguez JL, et al. Single-cell dissection of cellular components and interactions shaping the tumor immune phenotypes in ovarian cancer. Cancer Cell. 2021;39:928–e944926.
50. Chen H, Molberg K, Strickland AL, Castrillon DH, Carrick K, Jiang Q, Niu S, Rivera-Colon G, Gwin K, Hinson S, et al. PD-L1 expression and CD8 + Tumor-infiltrating lymphocytes in different types of Tubo-ovarian carcinoma and their prognostic value in High-grade serous carcinoma. Am J Surg Pathol. 2020;44:1050–60.
51. Kandalaft LE, Dangaj Laniti D, Coukos G. Immunobiology of high-grade serous ovarian cancer: lessons for clinical translation. Nat Rev Cancer. 2022;22:640–56.
52. Pignata S, Bookman M, Sehouli J, Miller A, Penson RT, Taskiran C, Anderson C, Hietanen S, Myers T, Madry R, et al. Overall survival and patient-reported outcome results from the placebo-controlled randomized phase III IMagyn050/GOG 3015/ENGOT-OV39 trial of Atezolizumab for newly diagnosed stage III/IV ovarian cancer. Gynecol Oncol. 2023;177:20–31.
53. Moore KN, Bookman M, Sehouli J, Miller A, Anderson C, Scambia G, Myers T, Taskiran C, Robison K, Mäenpää J, et al. Atezolizumab, bevacizumab, and chemotherapy for newly diagnosed stage III or IV ovarian cancer: Placebo-Controlled randomized phase III trial (IMagyn050/GOG 3015/ENGOT-OV39). J Clin Oncol. 2021;39:1842–55.
54. Huntimer ED, Halaweish FT, Chase CC. Proliferative activity of Echinacea angustifolia root extracts on cancer cells: interference with doxorubicin cytotoxicity. Chem Biodivers. 2006;3:695–703.
55. de la Martin L, Westbom-Fremer S, Arildsen NS, Hartman L, Malander S, Kannisto P, Måsbäck A, Hedenfalk I. PD-1/PD-L1 expression and tumor-infiltrating lymphocytes are prognostically favorable in advanced high-grade serous ovarian carcinoma. Virchows Arch. 2020;477:83–91.
56. Wouters MC, Komdeur FL, Workel HH, Klip HG, Plat A, Kooi NM, Wisman GB, Mourits MJ, Arts HJ, Oonk MH, et al. Treatment regimen, surgical outcome, and T-cell differentiation influence prognostic benefit of Tumor-Infiltrating lymphocytes in High-Grade serous ovarian cancer. Clin Cancer Res. 2016;22:714–24.
57. Miller BC, Sen DR, Al Abosy R, Bi K, Virkud YV, LaFleur MW, Yates KB, Lako A, Felt K, Naik GS, et al. Subsets of exhausted CD8(+) T cells differentially mediate tumor control and respond to checkpoint Blockade. Nat Immunol. 2019;20:326–36.
58. Egen JG, Ouyang W, Wu LC. Human Anti-tumor immunity: insights from immunotherapy clinical trials. Immunity. 2020;52:36–54.
59. Bhatt D, Kang B, Sawant D, Zheng L, Perez K, Huang Z, Sekirov L, Wolak D, Huang JY, Liu X et al. STARTRAC analyses of ScRNAseq data from tumor models reveal T cell dynamics and therapeutic targets. J Exp Med 2021, 218.
60. Wu TD, Madireddi S, de Almeida PE, Banchereau R, Chen YJ, Chitre AS, Chiang EY, Iftikhar H, O'Gorman WE, Au-Yeung A, et al. Peripheral T cell expansion predicts tumour infiltration and clinical response. Nature. 2020;579:274–8.
61. Yost KE, Satpathy AT, Wells DK, Qi Y, Wang C, Kageyama R, McNamara KL, Granja JM, Sarin KY, Brown RA, et al. Clonal replacement of tumor-specific T cells following PD-1 Blockade. Nat Med. 2019;25:1251–9.
62. Lin HW, Chiang YC, Sun NY, Chen YL, Chang CF, Tai YJ, Chen CA, Cheng WF. CHI3L1 results in poor outcome of ovarian cancer by promoting properties of stem-like cells. Endocr Relat Cancer. 2019;26:73–88.
63. Taifour T, Attalla SS, Zuo D, Gu Y, Sanguin-Gendreau V, Proud H, Solymoss E, Bui T, Kuasne H, Papavasiliou V, et al. The tumor-derived cytokine Chi3l1 induces neutrophil extracellular traps that promote T cell exclusion in triple-negative breast cancer. Immunity. 2023;56:2755–e27722758.
64. Ji S, Yu H, Zhou D, Fan X, Duan Y, Tan Y, Lang M, Shao G. Cancer stem cell-derived CHI3L1 activates the MAF/CTLA4 signaling pathway to promote immune escape in triple-negative breast cancer. J Transl Med. 2023;21:721.
65. He M, Kok M. Chi3l1: new kid on the T cell Blockade. Immunity. 2023;56:2672–4.
66. Zhu X, Sun L, Song N, He W, Xie B, Hu J, Zhang J, Yang J, Dai J, Bian D, et al. Safety and effectiveness of neoadjuvant PD-1 inhibitor (toripalimab) plus

chemotherapy in stage II-III NSCLC (LungMate 002): an open-label, single-arm, phase 2 trial. BMC Med. 2022;20:493.

67. Ma B, Akosman B, Kamle S, Lee CM, He CH, Koo JS, Lee CG, Elias JA. CHI3L1 regulates PD-L1 and anti-CHI3L1-PD-1 antibody elicits synergistic antitumor responses. J Clin Invest 2021, 131.
68. Whitwell HJ, Worthington J, Blyuss O, Gentry-Maharaj A, Ryan A, Gunu R, Kalsi J, Menon U, Jacobs I, Zaikin A, Timms JF. Improved early detection of ovarian cancer using longitudinal multimarker models. Br J Cancer. 2020;122:847–56.
69. Thöm I, Andritzky B, Schuch G, Burkholder I, Edler L, Johansen JS, Bokemeyer C, Schumacher U, Laack E. Elevated pretreatment serum concentration of YKL-40-An independent prognostic biomarker for poor survival in patients with metastatic nonsmall cell lung cancer. Cancer. 2010;116:4114–21.
70. Chen CC, Pekow J, Llado V, Kanneganti M, Lau CW, Mizoguchi A, Mino-Kenudson M, Bissonnette M, Mizoguchi E. Chitinase 3-like-1 expression in colonic epithelial cells as a potentially novel marker for colitis-associated neoplasia. Am J Pathol. 2011;179:1494–503.
71. Guan B, Li M, Cui D, Shen C, Hao Z, Li X. Single-cell transcriptomic analysis in clear cell renal cell carcinoma: Deciphering the role of APP within the tumour microenvironment. J Cell Mol Med. 2024;28:e18186.
72. Ma R, Zhou X, Zhai X, Wang C, Hu R, Chen Y, Shi L, Fang X, Liao Y, Ma L, et al. Single-cell RNA sequencing reveals immune cell dysfunction in the peripheral blood of patients with highly aggressive gastric cancer. Cell Prolif. 2024;57:e13591.
73. Jiang L, Zhao X, Li Y, Hu Y, Sun Y, Liu S, Zhang Z, Li Y, Feng X, Yuan J, et al. The tumor immune microenvironment remodeling and response to HER2-targeted therapy in HER2-positive advanced gastric cancer. IUBMB Life. 2024;76:420–36.
74. Li M, Duan X, Xiao Y, Yuan M, Zhao Z, Cui X, Wu D, Shi J. BUB1 is identified as a potential therapeutic target for pancreatic cancer treatment. Front Public Health. 2022;10:900853.
75. Song H, Lou C, Ma J, Gong Q, Tian Z, You Y, Ren G, Guo W, Wang Y, He K, Xiao M. Single-Cell transcriptome analysis reveals changes of tumor immune microenvironment in oral squamous cell carcinoma after chemotherapy. Front Cell Dev Biol. 2022;10:914120.
76. Wan Y, Jiang J, Chen M, Han X, Zhong L, Xiao F, Liu J, Liu J, Li H, Huang H, Hou J. Unravelling the imbalanced Th17-like cell differentiation by single-cell RNA sequencing in multiple myeloma. Int Immunopharmacol. 2023;124:110852.
77. Wu C, Wang X, Shang H, Wei H. Construction of a Humanized PBMC-PDX Model to Study the Efficacy of a Bacterial Marker in Lung Cancer Immunotherapy. Dis Markers 2022;2022:1479246.
78. Lin X, Zeng T, Lin J, Zhang Q, Cheng H, Fang S, Lin S, Chen Y, Xu Y, Lin J. Establishment of humanized tumor microenvironment mouse models based on the injection of peripheral blood mononuclear cells and IFN-γ to evaluate the efficacy of PD-L1/PD-1-targeted immunotherapy. Cancer Biol Ther. 2020;21:130–8.
79. Lin S, Huang G, Cheng L, Li Z, Xiao Y, Deng Q, Jiang Y, Li B, Lin S, Wang S, et al. Establishment of peripheral blood mononuclear cell-derived humanized lung cancer mouse models for studying efficacy of PD-L1/PD-1 targeted immunotherapy. MAbs. 2018;10:1301–11.
80. R Core Team R. R: A language and environment for statistical computing. 2013.
81. Hao Y, Hao S, Andersen-Nissen E, Mauck WM 3rd, Zheng S, Butler A, Lee MJ, Wilk AJ, Darby C, Zager M, et al. Integrated analysis of multimodal single-cell data. Cell. 2021;184:3573–e35873529.
82. Aran D, Looney AP, Liu L, Wu E, Fong V, Hsu A, Chak S, Naikawadi RP, Wolters PJ, Abate AR, et al. Reference-based analysis of lung single-cell sequencing reveals a transitional profibrotic macrophage. Nat Immunol. 2019;20:163–72.
83. Wu T, Hu E, Xu S, Chen M, Guo P, Dai Z, Feng T, Zhou L, Tang W, Zhan L, et al. ClusterProfiler 4.0: A universal enrichment tool for interpreting omics data. Innov (Camb). 2021;2:100141.
84. Hänzelmann S, Castelo R, Guinney J. GSVA: gene set variation analysis for microarray and RNA-seq data. BMC Bioinformatics. 2013;14:7.
85. Liberzon A, Birger C, Thorvaldsdóttir H, Ghandi M, Mesirov JP, Tamayo P. The molecular signatures database (MSigDB) hallmark gene set collection. Cell Syst. 2015;1:417–25.
86. Aibar S, González-Blas CB, Moerman T, Huynh-Thu VA, Imrichova H, Hulselmans G, Rambow F, Marine JC, Geurts P, Aerts J, et al. SCENIC: single-cell regulatory network inference and clustering. Nat Methods. 2017;14:1083–6.
87. Jin S, Guerrero-Juarez CF, Zhang L, Chang I, Ramos R, Kuan CH, Myung P, Plikus MV, Nie Q. Inference and analysis of cell-cell communication using cellchat. Nat Commun. 2021;12:1088.
88. Bray NL, Pimentel H, Melsted P, Pachter L. Near-optimal probabilistic RNA-seq quantification. Nat Biotechnol. 2016;34:525–7.

## Publisher's note